

# Predictive design and performance analysis of lead-free $\text{CH}_3\text{NH}_3\text{SnI}_3$ -based perovskite solar cells through a combination of SCAPS-1D and machine learning based modelling

Tanvir Mahtab Khan <sup>a</sup>, Benjer Islam <sup>a</sup>, Md Mountasir Rahaman <sup>b</sup>, Mirza Md Shakil <sup>b</sup>, Md Ferdous Rahman <sup>c</sup>, Sheikh Rashel Al Ahmed <sup>a,\*</sup>

<sup>a</sup> Department of Electrical, Electronic and Communication Engineering, Pabna University of Science and Technology, Pabna, 6600, Bangladesh

<sup>b</sup> Department of Computer Science & Engineering, University of Asia Pacific, 74/A Green Rd, Dhaka, 1205, Bangladesh

<sup>c</sup> Advanced Energy Materials and Solar Cell Research Laboratory, Department of Electrical and Electronic Engineering, Begum Rokeya University, Rangpur, 5400, Bangladesh

## ARTICLE INFO

### Keywords:

$\text{CH}_3\text{NH}_3\text{SnI}_3$  absorber  
 $\text{ZnS}$  ETL  
 $\text{MoO}_3$  HTL  
SCAPS-1D  
Machine learning

## ABSTRACT

In this numerical research, the heterojunction Al/FTO/ZnS/ $\text{CH}_3\text{NH}_3\text{SnI}_3/\text{MoO}_3/\text{Au}$  solar cell structure is designed, and its photovoltaic (PV) characteristics are investigated using the SCAPS-1D simulator. Furthermore, a comparison of the PV output metrics of the  $\text{CH}_3\text{NH}_3\text{SnI}_3$ -based PSCs with several electron transport layers (ETLs) and hole transport layers (HTLs) is also presented in this research. From the outcomes, it is apparent that the proposed PSC with  $\text{ZnS}$  as ETL and  $\text{MoO}_3$  as HTL provides outstanding PV performances. Here, the influences of perovskite layer thickness, carrier density, bulk defect state, and defect density at both interfaces are examined. Additionally, the effects of operating temperature and back contact metal work function (WF) on PV outcomes are also evaluated. Furthermore, Nyquist plots and lattice mismatch calculations are introduced to analyze the charge recombination loss at both interfaces. The highest efficiency of 32.57 %, along with fill-factor (FF) of 87.58 %, open circuit voltage ( $V_{oc}$ ) of 1.08 V, and short circuit current density ( $J_{sc}$ ) of 34.36 mA/cm<sup>2</sup> are achieved for the suggested structure after optimizing all the physical parameters. Moreover, a linear regression machine learning (ML) algorithm is trained to analyze the influences of physical parameters of the  $\text{CH}_3\text{NH}_3\text{SnI}_3$  perovskite layer on the efficiency of the proposed structure. Among the eight features, the highest relative importance of 28.72 % is determined for defect density, which influences the device performance profoundly. In general, these findings can assist researchers in PV technology to fabricate low-cost, incredibly efficient, and Cd-free solar cells based on the  $\text{CH}_3\text{NH}_3\text{SnI}_3$  perovskite layer.

## 1. Introduction

In accordance with the expansion of contemporary civilizations, there has been a notable rise in the everyday consumption of energy resources. At present, fossil fuels contribute to the majority of the world's energy consumption, and in the near future, these resources will run out [1]. As it contaminates the atmosphere, therefore, the most difficult challenge is to build a sustainable energy source. In this case, particularly solar devices can be used as a substitute for traditional energy sources, since there is a great possibility that we can considerably lessen global warming through the use of renewable energy [2,3]. The major benefits of renewable energy are that it does not have any

negative environmental effects and is clean [4]. Right now, 90 % of the global renewable energy consumption is governed by first-generation crystalline silicon (Si)-based solar cells [5]. Although the efficiency of Si solar cells already reaches up to 25 %, their manufacturing costs are high [6]. Due to this, researchers in photovoltaic (PV) technology are looking for novel materials to create solar cells. Among the multiple kinds of solar cells, third-generation perovskite solar cells (PSCs) have been the focus of attention recently since they can be fabricated inexpensively while achieving high performance [7]. Further, perovskite substances have exceptional PV performance characteristics due to their large charge-carrier diffusion lengths, outstanding absorption capabilities, and suitable bandgap [8,9]. Despite the impressive outcomes of the

\* Corresponding author.

E-mail address: [rashel@pust.ac.bd](mailto:rashel@pust.ac.bd) (S.R.A. Ahmed).

present PSCs, the harmful heavy element lead (Pb) is found in the perovskite light harvesting layer [10]. Because of the toxicity and unstable behavior of the Pb-based PSCs, the broad commercial production is a major challenge [11]. Hence, without affecting the overall performance of the PV devices, researchers are working to substitute other environmentally friendly metallic ions instead of the harmful Pb [2]. In this case, tin (Sn)-based PSCs are becoming more and more prominent owing to their superior PV characteristics, favorable bandgap, outstanding performance, affordable manufacturing cost, and ecological compatibility [12,13].

Pb-free Methyl Ammonium Tin Iodide ( $\text{CH}_3\text{NH}_3\text{SnI}_3$ ) perovskite has emerged as an attractive replacement for Pb-based perovskite owing to its outstanding optoelectronic characteristics, including a direct bandgap of 1.3 eV, increased charge carrier mobility, excellent absorption capability, earth abundance, and simple fabrication process [14, 15]. The highest experimental efficiency of 6.4 % has been achieved till now for  $\text{CH}_3\text{NH}_3\text{SnI}_3$ -based PSCs, which is considerably lower than the Pb-based PSCs with an optimum power conversion efficiency (PCE) of 25.8 % [4,16]. Numerically, 23.57 % efficiency is obtained for the structure of ITO/SnO<sub>2</sub>/CH<sub>3</sub>NH<sub>3</sub>SnI<sub>3</sub>/CuSCN/Mo [17]. An efficiency of 24.82 % is achieved for the CH<sub>3</sub>NH<sub>3</sub>SnI<sub>3</sub>-based PSC with TiO<sub>2</sub> as ETL and CuI as HTL [18]. Recently, the CH<sub>3</sub>NH<sub>3</sub>SnI<sub>3</sub> PSC incorporating CdS as ETL and Cu<sub>2</sub>O as HTL obtained a PCE of 25.02 % [19]. Another study reports a highest efficiency of 25.05 % for the CH<sub>3</sub>NH<sub>3</sub>SnI<sub>3</sub>-based PSC with PCBM as ETL and CuI as HTL [20]. For the HTL-free structure of FTO/TiO<sub>2</sub>/CH<sub>3</sub>NH<sub>3</sub>SnI<sub>3</sub>/Ni, the highest PCE of 26.33 % has been achieved until now [8]. An n-i-p perovskite solar cell structure of FTO/TiO<sub>2</sub>/CH<sub>3</sub>NH<sub>3</sub>SnI<sub>3</sub>/CuO achieves an optimum PCE of 26.92 % [2]. The optimal PCE of 28.39 % is obtained for the CH<sub>3</sub>NH<sub>3</sub>SnI<sub>3</sub>-based PSC with TiO<sub>2</sub> as ETL and Cu<sub>2</sub>O as HTL [1]. Another study achieves an efficiency of 29.74 % for the PV cell architecture of FTO/TiO<sub>2</sub>/CH<sub>3</sub>NH<sub>3</sub>SnI<sub>3</sub>/CuSbS<sub>2</sub>/back contact [21]. The efficiency of the CH<sub>3</sub>NH<sub>3</sub>SnI<sub>3</sub>-based PSCs, both in experimental and numerical contexts, remains lower than the Shockley-Queisser limits. Since, the perovskite materials are susceptible to accelerated decomposition in water, oxygen, light, heat, and other media, they are inherently unstable [22]. Most high-performance perovskites contain lead, which poses environmental and health risks [22,23]. Proper disposal and recycling strategies are required but remain challenging at scale. On the other hand, lead-free perovskites (e.g., tin-based) are often less efficient and less stable [23]. Tin-based perovskites are highly susceptible to oxidation, with Sn<sup>2+</sup> easily oxidizing to Sn<sup>4+</sup> upon exposure to oxygen or moisture [4,23]. This results in material degradation and loss of performance. The PSC based on CH<sub>3</sub>NH<sub>3</sub>SnI<sub>3</sub> is less thermally stable than its lead-based counterparts, making it unsuitable for high-temperature environments. The CH<sub>3</sub>NH<sub>3</sub>SnI<sub>3</sub>-based PSC generally exhibit lower PCEs compared to lead-based perovskites due to higher defect densities, faster carrier recombination, and reduced stability [4,24].

Also, the reason behind this reduced performance is the misalignment in energy bands between the absorber, charge transport layers, and electrodes and the improper lattice mismatch between various layers [19]. Therefore, in order to maximize cell performance, it is essential to meticulously investigate the design techniques, material properties, and charge transfer mechanism of the heterostructure PSCs. The PV output characteristics of the PSC can be improved by maintaining appropriate band arrangement at the ETL/perovskite and perovskite/HTL interfaces, since it reduces the rate of recombination at the front and back surfaces, respectively [25]. Moreover, the incorporation of HTL as the back-surface passivation layer generates a built-in electric field at the perovskite/HTL junction, which diminishes the carrier recombination at the rear surface [26]. As a result, the PV performance metrics of the solar cell devices increased substantially.

Nowadays, machine learning (ML) is a good choice in the field of PV technology to evaluate the influence of the physical properties of solar devices on their performance parameters [25,27–31]. It facilitates obtaining the best performance characteristics of a solar device by

optimizing the physical parameters of various layers. The performance parameters and relative importance of material attributes of several solar devices have been predicted and evaluated by performing ML analysis, as reported in previous studies [27–31]. Their study reports that ML can be useful in predicting optimized physical parameters for the design and fabrication of highly efficient solar devices.

In this work, zinc sulfide (ZnS) is employed as an appropriate ETL instead of the conventionally used cadmium sulfide (CdS) with the CH<sub>3</sub>NH<sub>3</sub>SnI<sub>3</sub> perovskite layer. The remarkable and distinctive properties of the ZnS ETL, including a tunable bandgap ranging between 2.6 and 3.8 eV, non-toxicity, low cost, and greater conductivity, have made it a viable ETL in solar panel technology [27]. Further, a “cliff-like” band formation is formed at the CdS/CH<sub>3</sub>NH<sub>3</sub>SnI<sub>3</sub> interface, which increases the non-radiative charge recombination at the ETL/perovskite interface and consequently degrades the PV performance [32]. On the other hand, a “spike-like” band orientation forms at the ZnS/CH<sub>3</sub>NH<sub>3</sub>SnI<sub>3</sub> interface, which facilitates the easier passage of electrons from the CH<sub>3</sub>NH<sub>3</sub>SnI<sub>3</sub> absorber to the front contact through the ZnS ETL [32]. As a result, the carrier recombination at the front surface diminishes and boosts the output metrics of the suggested PSC. Additionally, three HTLs, including MoO<sub>3</sub>, CuSCN, and NiO, have been sandwiched between the perovskite layer and rear electrode. Among the three HTLs, MoO<sub>3</sub> provides appropriate band alignment with the perovskite layer and shows outstanding PV performance. This happens because the smaller valence band offset (VBO) and large conduction band offset (CBO) at the CH<sub>3</sub>NH<sub>3</sub>SnI<sub>3</sub>/MoO<sub>3</sub> interface allow the smooth transportation of holes and block the flows of minority electrons from the CH<sub>3</sub>NH<sub>3</sub>SnI<sub>3</sub> layer to the rear electrode through the MoO<sub>3</sub> HTL [33]. Consequently, an improved solar cell performance is achieved for the proposed structure. Furthermore, MoO<sub>3</sub> HTL offers several extraordinary optoelectronic benefits, such as a favorable band gap, higher carrier mobility, good stability, and extended diffusion length [34]. These features make the MoO<sub>3</sub> material an emerging viable alternative in PV technology.

In this numerical analysis, the SCAPS-1D simulator is employed to design and examine the PV characteristics of the CH<sub>3</sub>NH<sub>3</sub>SnI<sub>3</sub>-based PSC of the structure of Al/FTO/ZnS/CH<sub>3</sub>NH<sub>3</sub>SnI<sub>3</sub>/MoO<sub>3</sub>/Au. Herein, various physical parameters, including thickness, doping density, bulk and interface defects, temperature, and metal work function, have been examined to design the economical and highly efficient CH<sub>3</sub>NH<sub>3</sub>SnI<sub>3</sub>-based PSC. Subsequently, we trained a supervised linear regression machine learning algorithm to predict the efficiency of the proposed structure by analyzing a large set of data.

## 2. Device architecture and methods

### 2.1. SCAPS-1D simulation

In this work, the SCAPS-1D program is used to model and simulate a CH<sub>3</sub>NH<sub>3</sub>SnI<sub>3</sub>-based PSC with ZnS ETL and MoO<sub>3</sub> HTL. The SCAPS encompass a foundational set of equations, which include the continuity equations, the transport equations, and Poisson's equation. The evolution of hole and electron densities through recombination, generation, and transport processes is explained by the transport and continuity equations. Poisson's equation demonstrates how local charge densities impact the electrostatic potential [35].

$$\frac{d^2}{dx^2} \Psi(x) = \frac{e}{\epsilon_0 \epsilon_r} p(x) - n(x) + N_D - N_A + \rho_p - \rho_n \quad (1)$$

$$\frac{dJ_n}{dx} = \frac{dJ_p}{dx} = G - R \quad (2)$$

where e is electrical charge,  $\rho_n$  and  $\rho_p$  are the electron and hole distribution,  $\Psi(x)$  is electrostatic potential, G is the generation rate, R is the rate of recombination,  $N_D$  and  $N_A$  are the densities of donors and acceptors, respectively.

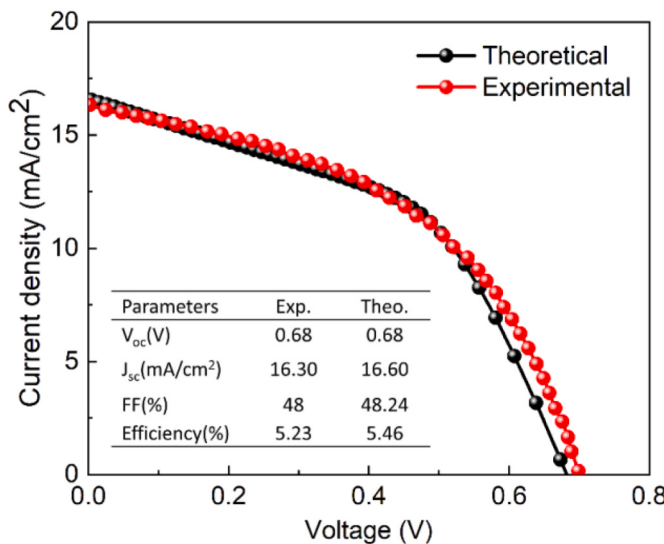


Fig. 1. Simulation and experimental J-V curves of  $\text{CH}_3\text{NH}_3\text{SnI}_3$ -based PSCs.

$$J_n = D_n \frac{dn}{dx} + \mu_n n \frac{d\Phi}{dx} \quad (3)$$

$$J_p = D_p \frac{dp}{dx} + \mu_p p \frac{d\Phi}{dx} \quad (4)$$

where  $J_n$  and  $J_p$  are the electron and hole current densities.  $D_p$  and  $D_n$  are the diffusion coefficient of holes and electrons, respectively.  $\Phi$  represents the built-in potential, and  $\mu_n$  and  $\mu_p$  are the electron and hole mobilities, respectively.

Initially, to validate the reliability of this numerical approach, the experimental outcomes [24] are reproduced using the SCAPS-1D simulator. The J-V curve and the PV performance parameters of the experimental and simulation outputs are depicted in Fig. 1 and (inset). It is clear from the demonstration that the numerical results are nearly identical to the published experimental results [24], thereby validating the reliability of this SCAPS-1D simulator.

After stating the reliability of the SCAPS-1D software, herein, we have designed a new PV heterostructure of Al/FTO/ZnS/ $\text{CH}_3\text{NH}_3\text{SnI}_3$ /MoO<sub>3</sub>/Au and the simplified diagram is demonstrated in Fig. 2(a). In this configuration, a 1-μm-thick  $\text{CH}_3\text{NH}_3\text{SnI}_3$  layer serves as the light harvesting layer, a 0.1-μm-thick MoO<sub>3</sub> layer functions as the HTL, and a 0.05 μm thick ZnS layer acts as the ETL. Further, FTO is employed as the transparent conducting oxide (TCO) layer. Aluminum (Al) and gold (Au) are used as the front and rear electrodes, with WF of 4.06 eV and 5.47 eV, respectively [36]. The physical parameters for various materials,

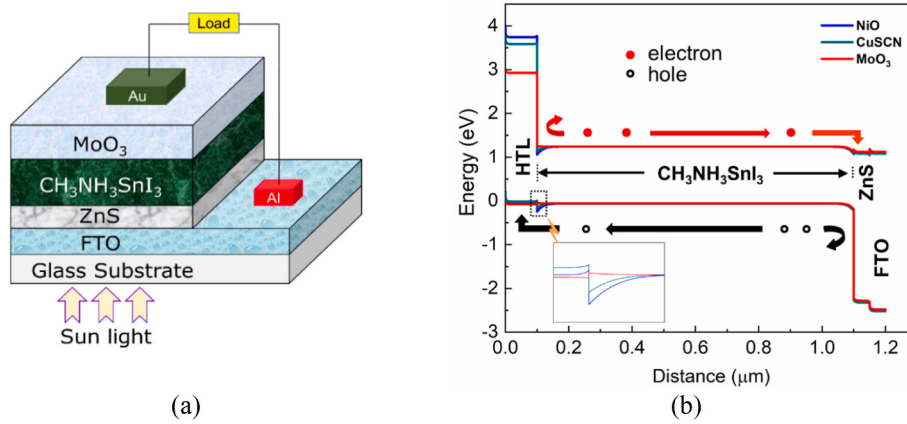


Fig. 2. (a) Schematic and (b) energy band demonstration of the mentioned PSC.

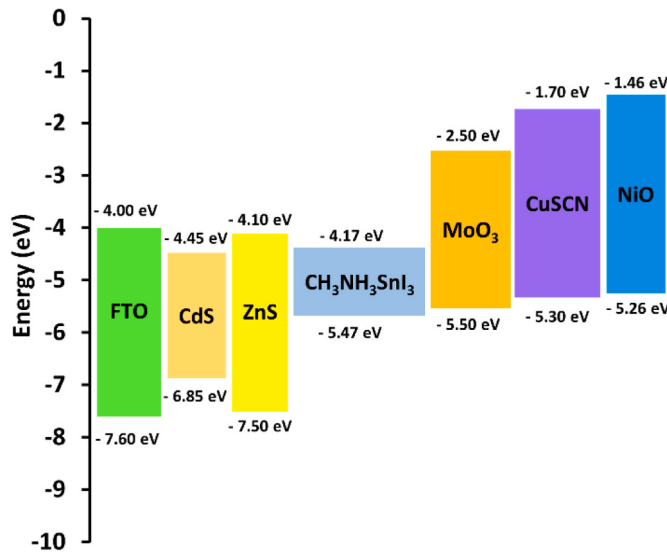
Table 1  
Physical parameters used for different layers in the suggested  $\text{CH}_3\text{NH}_3\text{SnI}_3$ -based PSC [1,8,19,27,34,37–39].

Parameters (unit)	n + -type Window (FTO)	n-type Buffer (CdS)	n-type Buffer (ZnS)	p-type Absorber ( $\text{CH}_3\text{NH}_3\text{SnI}_3$ )	p + -type HTL (MoO <sub>3</sub> )	p + -type HTL (CuSCN)	p + -type HTL (NiO)
Thickness (μm)	0.05	0.05	0.05	1.0*	0.1	0.1	0.1
Band gap (eV)	3.6 [34]	2.4 [22]	3.4 [31]	1.3 [51]	3.00 [34]	3.60 [36]	3.8 [36]
Electron affinity (eV)	4 [34]	4.45 [22]	4.1 [31]	4.17 [51]	2.50 [34]	1.70 [36]	1.46 [36]
Dielectric permittivity (relative)	9 [34]	9 [22]	9 [31]	8.2 [1]	12.50 [34]	10 [35]	10.7 [34]
CB effective DOS (cm <sup>-3</sup> )	$2.20 \times 10^{18}$ [34] [22]	$2.20 \times 10^{18}$ [31]	$2.20 \times 10^{18}$ [31]	$10^{18}$ [1]	$2.20 \times 10^{18}$ [34]	$2.20 \times 10^{19}$ [36]	$2.8 \times 10^{19}$ [36]
VB effective DOS (cm <sup>-3</sup> )	$1.80 \times 10^{19}$ [34] [22]	$1.80 \times 10^{19}$ [31]	$1.80 \times 10^{19}$ [31]	$10^{18}$ [1]	$1.80 \times 10^{19}$ [34]	$1.80 \times 10^{18}$ [36]	$1.0 \times 10^{19}$ [36]
Electron mobility (cm <sup>2</sup> /V-s)	100 [34]	100 [22]	100 [31]	1.6 [4]	25 [34]	100 [36]	12 [36]
Hole mobility (cm <sup>2</sup> /V-s)	25 [34]	25 [22]	25 [31]	1.6 [4]	100 [34]	25 [36]	2.8 [36]
Donor density N <sub>D</sub> (cm <sup>-3</sup> )	$10^{18}$ [34]	$10^{18}$ [22]	$10^{18}$	0	0	0	0
Acceptor density N <sub>A</sub> (cm <sup>-3</sup> )	0	0	0	$10^{17*}$ [8]	$10^{18}$ [34]	$10^{18}$ [36]	$10^{18}$ [36]
Defect type		Neutral [1,19]	Neutral [1,19]	Neutral [1,19]	Neutral [1,19]	Neutral [1,19]	Neutral [1,19]
Energetic distribution		Gaussian	Gaussian	Gaussian	Gaussian	Gaussian	Gaussian
Defect density (cm <sup>-3</sup> )		$10^{15}$ [22]	$10^{15}$	$10^{14*}$ [8]	$10^{15}$ [34]	$10^{15}$	$10^{15}$ [34]

**Table 2**

Defect parameters at absorber/ETL and HTL/absorber interfaces.

Parameters (unit)	CH <sub>3</sub> NH <sub>3</sub> SnI <sub>3</sub> /ZnS interface	MoO <sub>3</sub> /CH <sub>3</sub> NH <sub>3</sub> SnI <sub>3</sub> interface
Defect type	Neutral	Neutral
Capture cross-section of electrons (cm <sup>2</sup> )	10 <sup>-19</sup>	10 <sup>-19</sup>
Capture cross-section of holes (cm <sup>2</sup> )	10 <sup>-19</sup>	10 <sup>-19</sup>
Reference for defect energy level E <sub>t</sub>	Above the highest E <sub>v</sub>	Above the highest E <sub>v</sub>
Energy with respect to reference (eV)	0.6	0.6
Total density (cm <sup>-2</sup> )	10 <sup>12</sup>	10 <sup>12</sup>

**Fig. 3.** Energy level illustration of the proposed heterostructure PSC.

derived from prior experimental and numerical works, have been utilized to maximize the suggested CH<sub>3</sub>NH<sub>3</sub>SnI<sub>3</sub> PV devices, as detailed in **Table 1** [1,8,19,27,34,37–39]. Again, the interface parameters for CH<sub>3</sub>NH<sub>3</sub>SnI<sub>3</sub>/ETL and HTL/CH<sub>3</sub>NH<sub>3</sub>SnI<sub>3</sub> are provided in **Table 2**. Furthermore, the lighting conditions used in this theoretical analysis is under AM 1.5G standard illumination (100 mW/cm<sup>2</sup> irradiations) at 300K temperature, which is identical to the experimental condition [24].

The band diagram of the PSC at thermal equilibrium is depicted in **Fig. 2(b)**. This diagram illustrates the energy levels of the conduction band (E<sub>c</sub>), and valence band (E<sub>v</sub>) across the different layers of the device. A key observation in the band diagram is the higher conduction band energy level (E<sub>c</sub>) in the HTL compared to the absorber layer. This configuration is critical as it creates a potential barrier that facilitates the efficient extraction of holes while blocking electrons, thereby reducing recombination losses at the junction between the HTL and the perovskite [34,37]. The band alignment is designed to optimize charge carrier separation and transport, ensuring improved overall device performance.

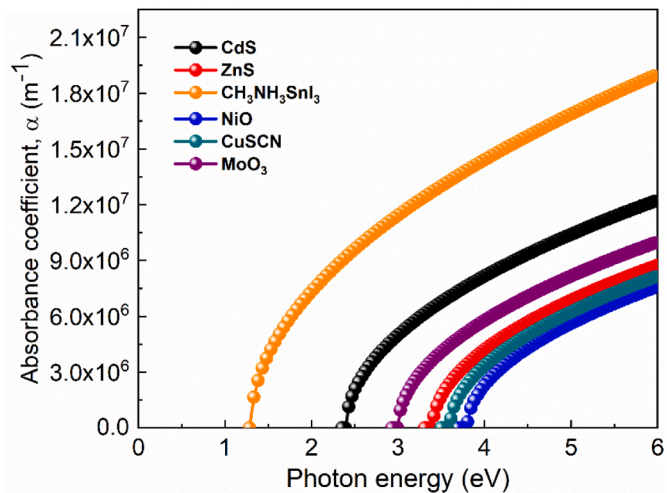
**Fig. 3** depicts the energy level of the CH<sub>3</sub>NH<sub>3</sub>SnI<sub>3</sub> perovskite layer with various ETLs (CdS, ZnS) and HTLs (MoO<sub>3</sub>, CuSCN, and NiO). Two different band offsets, namely CBO and VBO, are produced at the interface [40].

$$\Delta E_c = \Delta \chi \quad (5)$$

$$\Delta E_v = \Delta E_g - \Delta E_c \quad (6)$$

where  $\Delta E_g$  is defined as the difference in band gaps between the interface materials, whereas  $\Delta \chi$  is the deviation in electron affinities between the two elements.

To ensure efficient hole movement from the perovskite to the rear electrode across the HTL, the CBO at the CH<sub>3</sub>NH<sub>3</sub>SnI<sub>3</sub>/HTL interface should be positive, while the VBO should be nearly zero or negative [26]. The CBO values for MoO<sub>3</sub>, CuSCN, and NiO have been found to be 1.67 eV, 2.47 eV, and 2.71 eV, respectively. Their corresponding VBOs are -0.03 eV, 0.17 eV, and 0.21 eV. It is evident that the VBOs at the CH<sub>3</sub>NH<sub>3</sub>SnI<sub>3</sub>/NiO and CH<sub>3</sub>NH<sub>3</sub>SnI<sub>3</sub>/CuSCN interfaces are higher than the VBO at the CH<sub>3</sub>NH<sub>3</sub>SnI<sub>3</sub>/MoO<sub>3</sub> interface. The nearly zero VBO at the CH<sub>3</sub>NH<sub>3</sub>SnI<sub>3</sub>/MoO<sub>3</sub> interface may enable easier hole transport, thereby enhancing overall solar cell performance. Ensuring a small CBO at the ETL/absorber interface is crucial for efficient electron transfer from the perovskite to the front electrode across the ETL [41]. All the CBO and VBO values at the interfaces are listed in **Table 3**. It is found to be -0.28 eV CBO at the CdS/CH<sub>3</sub>NH<sub>3</sub>SnI<sub>3</sub> junction and 0.07 eV at the ZnS/CH<sub>3</sub>NH<sub>3</sub>SnI<sub>3</sub> junction. Therefore, it is evident that for smooth transportation of electrons, ZnS is a suitable candidate for ETL.

**Fig. 4.** Absorbance coefficient with regards to photon energy for CH<sub>3</sub>NH<sub>3</sub>SnI<sub>3</sub> absorber, various ETLs, and HTLs.**Table 3**Resultant parameters of CH<sub>3</sub>NH<sub>3</sub>SnI<sub>3</sub> PSCs with numerous ETLs and HTLs.

Configurations	CBO (eV)	VBO (eV)	V <sub>oc</sub> (V)	J <sub>sc</sub> (mA/cm <sup>2</sup> )	FF (%)	Efficiency (%)
Al/FTO/CdS/CH <sub>3</sub> NH <sub>3</sub> SnI <sub>3</sub> /Au	-0.28		0.96	27.28	80.99	21.17
Al/FTO/ZnS/CH <sub>3</sub> NH <sub>3</sub> SnI <sub>3</sub> /Au	0.07		1.02	30.85	83.87	26.45
Al/FTO/ZnS/CH <sub>3</sub> NH <sub>3</sub> SnI <sub>3</sub> /NiO/Au	2.71	0.21	1.04	31.86	85.69	28.49
Al/FTO/WS <sub>2</sub> /CH <sub>3</sub> NH <sub>3</sub> SnI <sub>3</sub> /CuSCN/Au	2.47	0.17	1.06	33.14	86.64	30.35
Al/FTO/ZnS/CH <sub>3</sub> NH <sub>3</sub> SnI <sub>3</sub> /MoO <sub>3</sub> /Au	1.67	-0.03	1.08	34.36	87.58	32.57

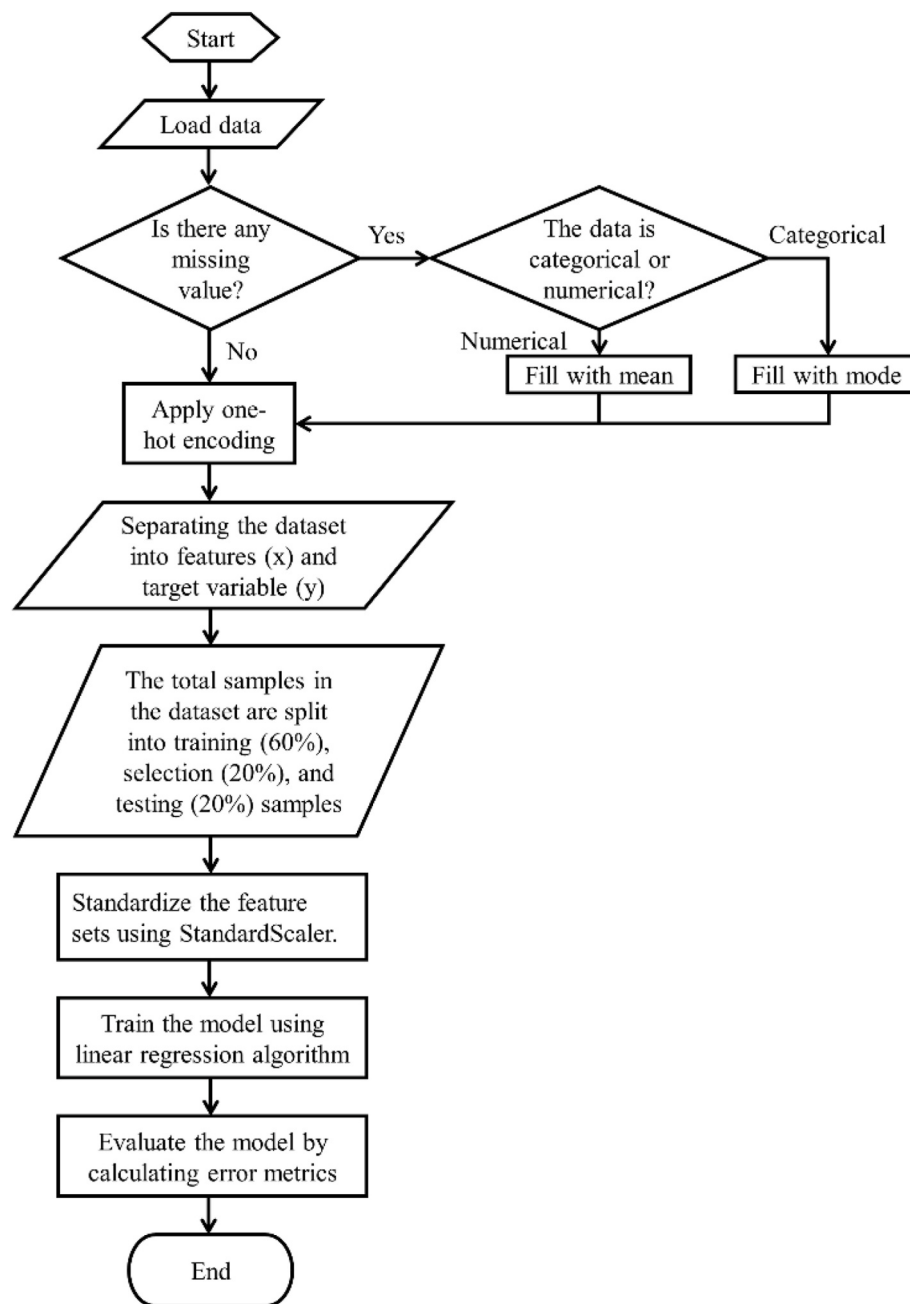


**Fig. 5.** A flowchart illustrates the algorithm used to execute the ML model.

Consequently, the integration of MoO<sub>3</sub> HTL and ZnS ETL at the rear and front of the perovskite is suggested to considerably boost the performance of CH<sub>3</sub>NH<sub>3</sub>Snl<sub>3</sub>-based PSCs.

The absorption coefficient ( $\alpha$ ) for individual materials of the suggested PSC is determined using the following equation [41].

$$\alpha = A_\alpha \sqrt{(hv - E_g)} \quad (7)$$

The energy bandgap ( $E_g$ ) and incident photon energy ( $hv$ ) are key parameters in the equation, with the pre-factor  $A_\alpha$  set at  $10^5 \text{ cm}^{-1}\text{eV}^{-1/2}$  for all elements in the recommended heterostructure PSC. The amount of light of a specific wavelength that can pass through an element without being captured is expressed by the absorption coefficient ( $\alpha$ ). Materials with low  $\alpha$  values absorb less light compared to those with higher values, and  $\alpha$  relies on both the element's bandgap and the light's wavelength [42]. Semiconductors show a sharp absorption edge, as light

with energy below the bandgap cannot excite electrons from the valence to the conduction band, resulting in no absorption. Fig. 4 illustrates the variation of  $\alpha$  with respect to photon energy for the CH<sub>3</sub>NH<sub>3</sub>Snl<sub>3</sub> absorber, various ETLs, and HTLs. It is evident from the figure that all elements have a high  $\alpha (> 10^5 \text{ cm}^{-1})$ , indicating excellent light capturing capabilities. The CH<sub>3</sub>NH<sub>3</sub>Snl<sub>3</sub> absorber exhibits the maximum  $\alpha$  among all the layers.

## 2.2. Machine learning

Machine learning (ML) is a branch of artificial intelligence (AI) that makes predictions using methods that learn from data. Due to the recent advancements in computing resources, devices, and data generation, ML strategies are gaining interest in the solar cell industry [43]. It could not be possible to test each substance and manufacturing condition since trial and error is costly, lengthy, and challenging. Thus, ML is a desirable

technique to advance the field of renewable energy resources. With the aid of the ML technique, massive amounts of data can be easily analyzed, and predictions can be easily made about the behaviour of physical parameters of PV devices [44]. This enhances the reliability and effectiveness of solar devices. Various algorithms, including decision tree, XGBoost, random forest (RF), Bayesian network, linear regression (LR), genetic algorithm, artificial neural network (ANN), etc., are the most frequently used techniques [43,45]. Among them, ANN, LR, and RF techniques perform most effectively in forecasting the physical parameters of the PV devices [43,45]. In terms of simplicity, LR is relatively simpler, and it has a significantly lower time delay [46,47]. Linear regression algorithm (LRA) is a fundamental machine learning method employed to predict a continuous target variable based on one or multiple input variables. According to the framework, there is a linear correlation between the dependent and independent variables. LRA can be expressed using the following equation:

$$y = w_1x_1 + w_2x_2 + w_3x_3 + \dots + w_nx_n + b \quad (8)$$

where  $w_1$  to  $w_n$  is the regression coefficient,  $x_1$  to  $x_n$  is the independent variable, and  $b$  is the error term. The precision of the LRA can be assessed by estimating the root mean square error (RMSE) and correlation coefficient ( $R^2$ ) [48], which are expressed as

$$MSE = \frac{1}{N} \sum_{i=1}^N (y_{i,target} - y_{i,prediction})^2 \quad (9)$$

$$RMSE = \sqrt{MSE} \quad (10)$$

$$R^2 = 1 - \frac{MSE}{\text{Var}(y_{target})} \quad (11)$$

where  $y_{i,target}$  and  $y_{i,prediction}$  is the  $i$ -th target and predicted value, and  $N$  is the number of samples.

In this study, Google Colab, the powerful tool for Python development, is used as integrated development environment (IDE) software. Additionally, several Python libraries are used for the efficient development of this model. The flowchart in Fig. 5 demonstrates the entire process of implementing and evaluating a linear regression model, from loading and preprocessing the data to training the model and finally assessing its performance.

### 3. Results and discussion

#### 3.1. Performance optimization of $\text{CH}_3\text{NH}_3\text{SnI}_3$ solar cell

In this research, the PV performance characteristics of the  $\text{CH}_3\text{NH}_3\text{SnI}_3$ -based PSCs, both with and without HTL, are evaluated. The effects of numerous ETLs (CdS and ZnS) and HTLs (MoO<sub>3</sub>, NiO, and CuSCN) on solar cell outcomes are demonstrated in Fig. 6, and the corresponding PV parameters with CBO and VBO values are listed in Table 3. The short-circuit current density voltage (J-V) and the variation of external quantum efficiency (EQE) regarding the wavelength for various configurations are presented in Fig. 6(a) and (b). In Fig. 6(a), it is apparent that the  $\text{CH}_3\text{NH}_3\text{SnI}_3$ -based PSC with ZnS ETL gives better performance compared to the CdS ETL. The efficiency of 26.45 %, along with FF of 83.87 %,  $J_{sc}$  of 30.45 mA/cm<sup>2</sup>, and  $V_{oc}$  of 1.02 V, is obtained

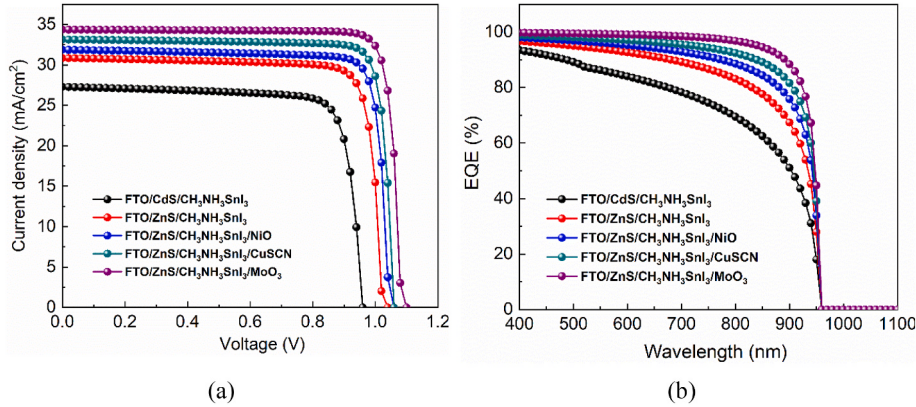


**Fig. 6.** (a) J-V characteristics and (b) EQE curves with regard to the wavelength of  $\text{CH}_3\text{NH}_3\text{SnI}_3$ -based PSCs without and with HTLs.

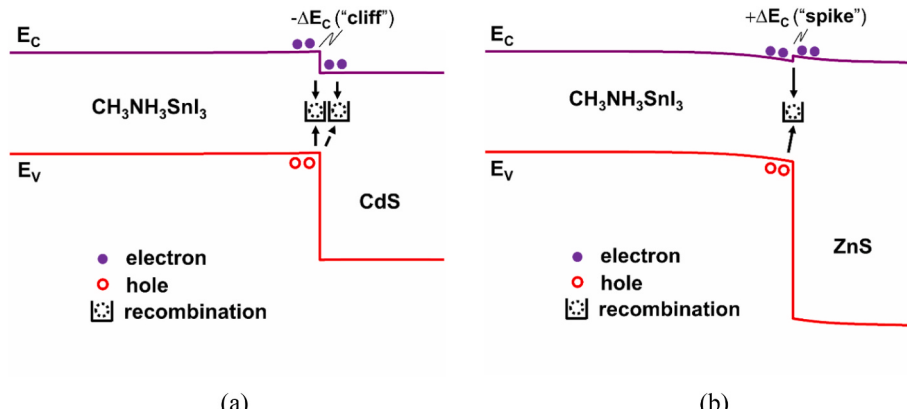


**Fig. 7.** Energy band demonstrations of  $\text{CH}_3\text{NH}_3\text{SnI}_3$  PSCs with CBO values of (a)  $-0.28$  eV at CdS/ $\text{CH}_3\text{NH}_3\text{SnI}_3$  interface and (b)  $+0.07$  eV at ZnS/ $\text{CH}_3\text{NH}_3\text{SnI}_3$  interface.

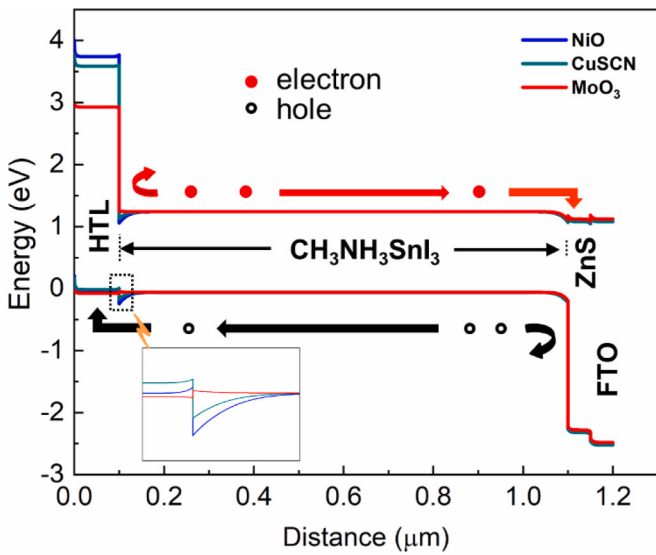


**Fig. 8.** Energy band visualization of  $\text{CH}_3\text{NH}_3\text{SnI}_3$  PSCs containing various HTLs.

for the  $\text{CH}_3\text{NH}_3\text{SnI}_3$ -based PSC with ZnS ETL. On the other hand, an efficiency of 21.17 %, along with FF of 80.99 %,  $J_{sc}$  of 27.28 mA/cm<sup>2</sup>, and  $V_{oc}$  of 0.96 V, is achieved for the CdS ETL structure. This performance enhancement may be due to the lower carrier recombination rate on the front surface. But these values are significantly lower in comparison to the device configuration with HTLs. Since the incorporation of a suitable rear surface passivation layer between the perovskite and rear contact reduces non-radiative carrier recombination, it therefore improves the efficiency of the suggested PSCs [27]. From Fig. 6(a) as well as Tables 3 and it is evident that the  $\text{CH}_3\text{NH}_3\text{SnI}_3$ -based PSC with MoO<sub>3</sub> HTL offers superior performances compared to the other two HTLs (CuSCN and NiO). The highest efficiency of 32.57 %, along with FF of 87.58 %,  $J_{sc}$  of 34.36 mA/cm<sup>2</sup>, and  $V_{oc}$  of 1.08 V, is achieved for the proposed structure with MoO<sub>3</sub> HTL.

The variation of EQE curve regarding the wavelength for the  $\text{CH}_3\text{NH}_3\text{SnI}_3$ -based PSCs with numerous configurations are illustrated in Fig. 6(b). The EQE delineates how many charge carriers a PV system may gather from irradiant photons with a specific energy [37]. From the figure, it is evident that the EQE curve for the ZnS/ $\text{CH}_3\text{NH}_3\text{SnI}_3$  configuration presents enhanced performance at longer wavelengths than the CdS/ $\text{CH}_3\text{NH}_3\text{SnI}_3$  configuration. Since the ZnS film's energy bandgap is larger than the CdS film, less light will be absorbed in the ZnS ETL. This makes it possible for more light, particularly at long wavelengths, to enter the  $\text{CH}_3\text{NH}_3\text{SnI}_3$  light-harvesting layer. Further, the appropriate band bending at the ZnS/ $\text{CH}_3\text{NH}_3\text{SnI}_3$  interface lowers the

carrier recombination loss. As a result, fewer photoinduced charge carriers can contribute to the current and improve the EQE at longer wavelengths. Additionally, as shown in the figure, the EQE curve for the  $\text{CH}_3\text{NH}_3\text{SnI}_3$ -based PSC with MoO<sub>3</sub> HTL outperforms the other HTLs (CuSCN, NiO) at longer wavelengths. The illustration shows that once the wavelength continues above 950 nm, the EQE drops to zero. This occurs as the incident rays cannot be captured by the  $\text{CH}_3\text{NH}_3\text{SnI}_3$  perovskite due to the reduced energy beneath the bandgap of the light-harvesting layer. Therefore, at wavelengths between 400 and 900 nm, the suggested PSC may produce the best outcomes.

The energy band diagram of the  $\text{CH}_3\text{NH}_3\text{SnI}_3$ -based PSC with CBO values of  $-0.28$  eV at the CdS/ $\text{CH}_3\text{NH}_3\text{SnI}_3$  interface and  $+0.07$  eV at the ZnS/ $\text{CH}_3\text{NH}_3\text{SnI}_3$  interface is presented in Fig. 7(a) and (b). Fig. 7(a) demonstrate that, due to the negative CBO values, a “cliff-like” band configuration forms at the CdS/ $\text{CH}_3\text{NH}_3\text{SnI}_3$  junction. As a result, electron-hole recombination takes place at the interface owing to the slight band bending, which degrades the PV output characteristics of the suggested PSC [49]. The activation energy ( $E_A$ ) for charge recombination can be estimated using the following equation [50].

$$E_A = E_{g,\text{absorber}} |CBO|, \quad (12)$$

where  $E_{g,\text{absorber}}$  is the band gap of the absorber layer. For “cliff-like” band structure,  $E_A < E_{g,\text{absorber}}$  [49]. This modest  $E_A$  at the CdS/ $\text{CH}_3\text{NH}_3\text{SnI}_3$  interface is generating an insignificant hole barrier. Consequently, the charge recombination takes place at the perovskite layer as well as at the ETL/perovskite interface [51]. By using the solid and dashed arrows, the enhanced charge recombination at the  $\text{CH}_3\text{NH}_3\text{SnI}_3$  layer and CdS/ $\text{CH}_3\text{NH}_3\text{SnI}_3$  interface is depicted in Fig. 7(a). Furthermore, the “spike-like” band formation at the ZnS/ $\text{CH}_3\text{NH}_3\text{SnI}_3$  interface is shown in Fig. 7(b). Since  $E_A > E_{g,\text{absorber}}$  for spike-like band formation, it creates an enhanced hole barrier [49]. As a result, hole transfer from the perovskite layer to the front surface is reduced, and ensures the effortless transfer of electrons from the perovskite to the front contact. Consequently, the suggested PSC provides significantly superior performance due to the lesser charge recombination at the interface.

The energy band illustration of the  $\text{CH}_3\text{NH}_3\text{SnI}_3$ -based PSC structure with three HTLs (MoO<sub>3</sub>, CuSCN, and NiO) is demonstrated in Fig. 8. The PV performance, along with the CBO and VBO values, are listed in Table 3. As we know, to ensure efficient hole transfer from the light harvesting layer to the rear electrode via the HTL, the CBO at the absorber/HTL interface should be positive, while the VBO should be nearly zero or negative [26]. Table 3 in our study shows that the proposed  $\text{CH}_3\text{NH}_3\text{SnI}_3$ -based PSC configuration with MoO<sub>3</sub> HTL has a significantly large CBO and negative VBO values. This will allow the efficient movement of holes from the perovskite layer to the rear electrode and reflect the minority electrons towards the front contact [32]. As a result, charge recombination at the back surface will be diminished. On the other hand, the comparatively high VBO values calculated at the

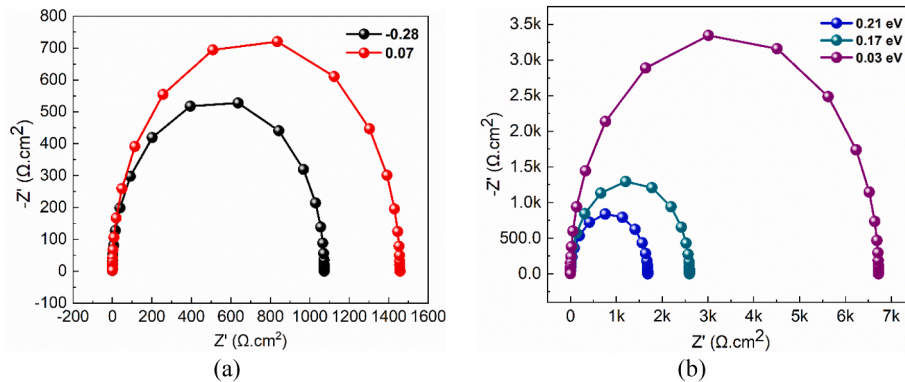


**Fig. 9.** Nyquist plot of  $\text{CH}_3\text{NH}_3\text{SnI}_3$  PSCs with different (a) CBO and (b) VBO values.

**Table 4**

Lattice mismatch of numerous ETLs and HTLs with  $\text{CH}_3\text{NH}_3\text{SnI}_3$  light harvesting layer.

Layers	Lattice parameters			Lattice mismatch (%)
	a ( $\text{\AA}$ )	b ( $\text{\AA}$ )	c ( $\text{\AA}$ )	
$\text{CH}_3\text{NH}_3\text{SnI}_3$ (absorber)	6.169	–	6.173	–
ZnS (ETL)	3.821	–	6.258	1.37
CdS (ETL)	–	–	6.749	8.92
$\text{MoO}_3$ (HTL)	7.122	5.374	5.565	10.29
$\text{CuSCN}$ (HTL)	3.850	–	10.938	46.29
NiO (HTL)	8.341	–	–	29.87

$\text{CH}_3\text{NH}_3\text{SnI}_3/\text{NiO}$  and  $\text{CH}_3\text{NH}_3\text{SnI}_3/\text{CuSCN}$  interfaces may prevent the holes from being transported from the perovskite to the back electrode via the HTL. Thus, the significant charge recombination at the back surface is responsible for the poor performance of the  $\text{CH}_3\text{NH}_3\text{SnI}_3$ -based PSC with CuSCN and NiO HTLs. Therefore, to achieve optimum solar cell performance,  $\text{MoO}_3$  material can be used as a potential HTL.

In addition, Nyquist plots are applied to analyze the influences of CBO and VBO on the PV characteristics of the proposed  $\text{CH}_3\text{NH}_3\text{SnI}_3$ -based PSCs. Nyquist plots are typically semicircle in shape [42]. The leftmost side of the semicircle implies the impedance at high frequency, and the right side signifies the impedance at low frequency [27]. The Nyquist plot for the CBO and VBO values is demonstrated in Fig. 9(a) and (b). From Fig. 9(a), it is evident that the semicircle for the CBO value of 0.07 eV at the ZnS/ $\text{CH}_3\text{NH}_3\text{SnI}_3$  interface is wider in diameter in contrast to the CBO value of  $-0.28$  eV at the CdS/ $\text{CH}_3\text{NH}_3\text{SnI}_3$  interface. Furthermore, Fig. 9(b) illustrates that the semicircle for VBO values of  $-0.03$  eV for the  $\text{CH}_3\text{NH}_3\text{SnI}_3$ -based PSC with  $\text{MoO}_3$  HTL has a greater diameter compared to the other HTLs (NiO and CuSCN) with VBO values of 0.21 and 0.17 eV. This is caused by efficient charge transfer and reduced possibilities of charge recombination at the ZnS/ $\text{CH}_3\text{NH}_3\text{SnI}_3$  and  $\text{CH}_3\text{NH}_3\text{SnI}_3/\text{MoO}_3$  interfaces [27,52,53]. Therefore, with the aim of designing and developing an exceptionally performing  $\text{CH}_3\text{NH}_3\text{SnI}_3$ -based PSC, in this study, ZnS ETL and  $\text{MoO}_3$  HTL are going to be used in the further analysis.

A possible method to assess the efficiency of the suggested  $\text{CH}_3\text{NH}_3\text{SnI}_3$ -based PSC structure is to determine the percentage lattice mismatch ( $\delta$ ) between the perovskite and other layers (ETLs and HTLs). Lattice mismatch generally explains the crystal homogeneity and irregularity of the materials within the heterojunction PV device [27]. The lattice mismatch ( $\delta$ ) can be determined using the equations below [27].

$$\delta = \frac{2|a_s - a_e|}{(a_s + a_e)} \times 100 \quad (13)$$

where  $a_e$  is the lattice constant of a layer and  $a_s$  is the lattice constant of the substrate on which an epitaxial layer grew on. The lattice parameters used in all the layers are derived from previous published reports [24,27, 34,54]. Table 4 lists the calculated  $\delta$  of various ETLs and HTLs with the  $\text{CH}_3\text{NH}_3\text{SnI}_3$  perovskite layer. From the table, it is evident that the value of  $\delta$  at the ZnS/ $\text{CH}_3\text{NH}_3\text{SnI}_3$  junction is substantially smaller than the value of  $\delta$  at the CdS/ $\text{CH}_3\text{NH}_3\text{SnI}_3$  junction. Similarly, the value of  $\delta$  at the  $\text{CH}_3\text{NH}_3\text{SnI}_3/\text{MoO}_3$  junction is substantially lower in comparison to the value of  $\delta$  at the  $\text{CH}_3\text{NH}_3\text{SnI}_3/\text{NiO}$  and  $\text{CH}_3\text{NH}_3\text{SnI}_3/\text{CuSCN}$  junctions. The large percentage  $\delta$  at the ETL/perovskite and perovskite/HTL interfaces generates sufficient trap states, which prompt nonradiative charge recombination at the interfaces [25]. As a result, the PV output metrics of the proposed PSC are degrading drastically. Thus, owing to the small  $\delta$  at the ZnS/ $\text{CH}_3\text{NH}_3\text{SnI}_3$  and  $\text{CH}_3\text{NH}_3\text{SnI}_3/\text{MoO}_3$  interfaces, the solar cell outcomes of the recommended structure improve.

### 3.2. Influences of thickness and carrier concentration of $\text{CH}_3\text{NH}_3\text{SnI}_3$ perovskite layer on output parameters

In this numerical study, the effects of the carrier concentration ( $N_A$ ) and thickness (W) of the  $\text{CH}_3\text{NH}_3\text{SnI}_3$  perovskite layer on the PV parameters of the suggested PSC are examined, and the corresponding outcomes are depicted in Fig. 10. Here, the values of  $N_A$  and W are adjusted between  $10^{13}$  and  $10^{20} \text{ cm}^{-3}$  and  $0.1$ – $1.5 \mu\text{m}$ , respectively. It is clearly obvious from the figure that all the performance parameters, including  $V_{oc}$ , FF, and PCE, are enhanced significantly with increasing the  $N_A$  of the  $\text{CH}_3\text{NH}_3\text{SnI}_3$  perovskite layer. This PV device's performance is enhanced as additional charge carriers are produced in the

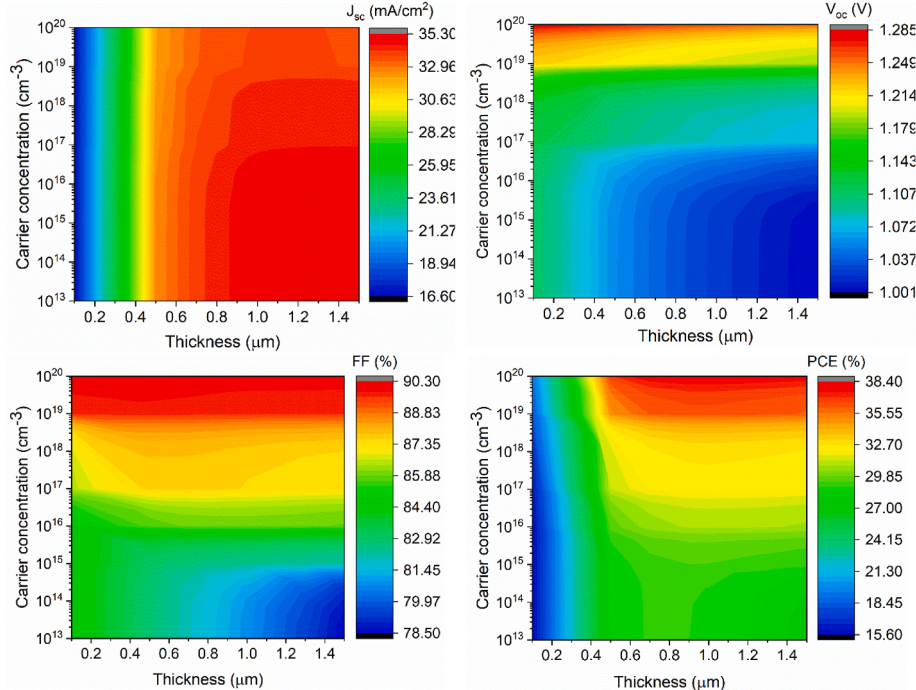
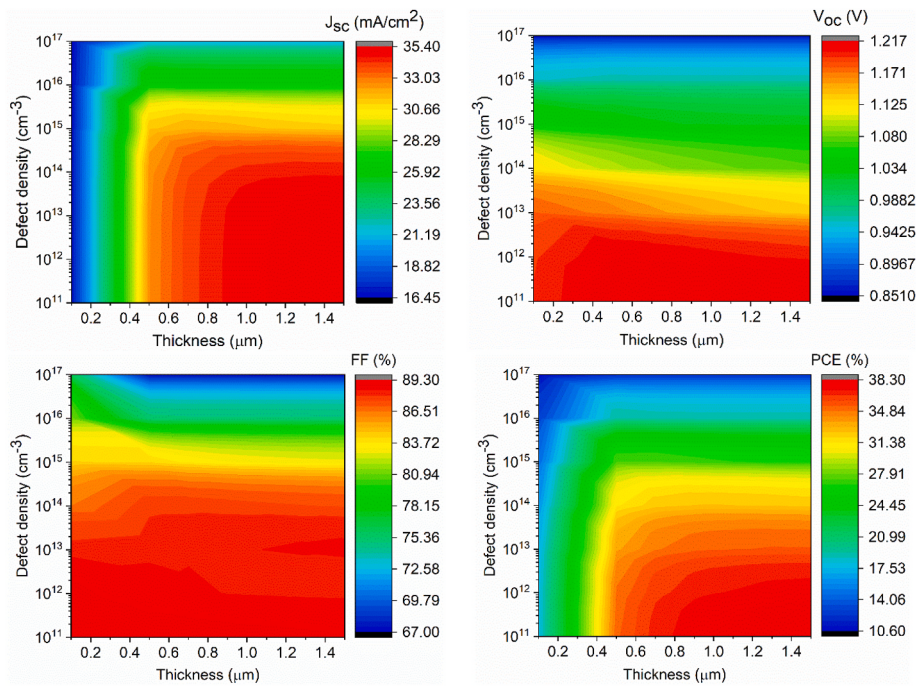


Fig. 10. Impacts of thickness and doping concentration on output metrics of designed PSC.



**Fig. 11.** Impacts of thickness and defect density on output metrics of the designed PSC.

perovskite layer due to an increase in carrier density [32]. On the other hand,  $J_{sc}$  is almost identical below the  $N_A$  of  $10^{16} \text{ cm}^{-3}$  and then degrades slightly. This little decrease in  $J_{sc}$  at the high doping state might be caused by the generation of hole traps at the p-type absorber, which enhances the recombination of hole traps with photoinduced electrons [33]. Further, it can be observed that the values of  $J_{sc}$  and PCE increase with growing W up to  $1.0 \mu\text{m}$  and then remain almost fixed. The value of FF increased for the perovskite layer thickness beyond  $0.7 \mu\text{m}$  and then dropped slightly. This reduction in FF is due to the rise of series resistance in the heterojunction PSC [25].

Furthermore, the figure shows that the value of  $V_{oc}$  falls with the rise in W. This occurs due to the generation of the dark saturation current ( $J_0$ ) [55]. The relationship between the  $V_{oc}$  and  $J_0$  can be described by the equation below [55].

$$V_{oc} = \frac{AK_B T}{q} \left[ \ln \left( 1 + \frac{J_{sc}}{J_0} \right) \right], \quad (14)$$

where  $K_B$ , T, and q are the Boltzmann constant, temperature, and charge, respectively. Equation (10) states that the  $V_{oc}$  is dependent on both  $J_{sc}$  and  $J_0$ . The  $V_{oc}$  is large at the thin perovskite layer. Conversely, the thick

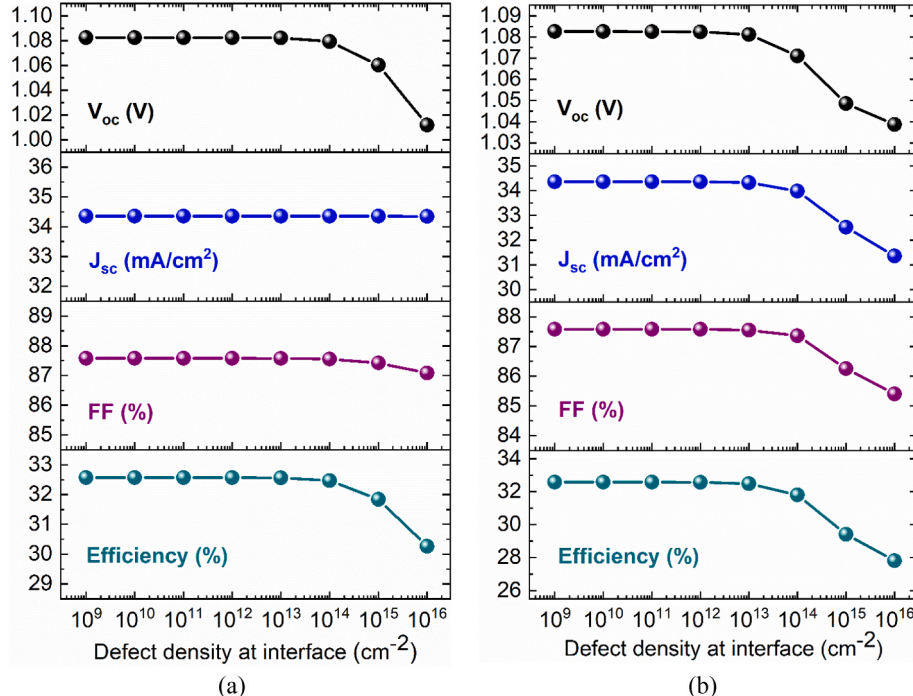


**Fig. 12.** Impacts of defect density at (a)  $\text{ZnS}/\text{CH}_3\text{NH}_3\text{SnI}_3$  and (b)  $\text{CH}_3\text{NH}_3\text{SnI}_3/\text{MoO}_3$  interfaces on performance metrics of the proposed PSC.

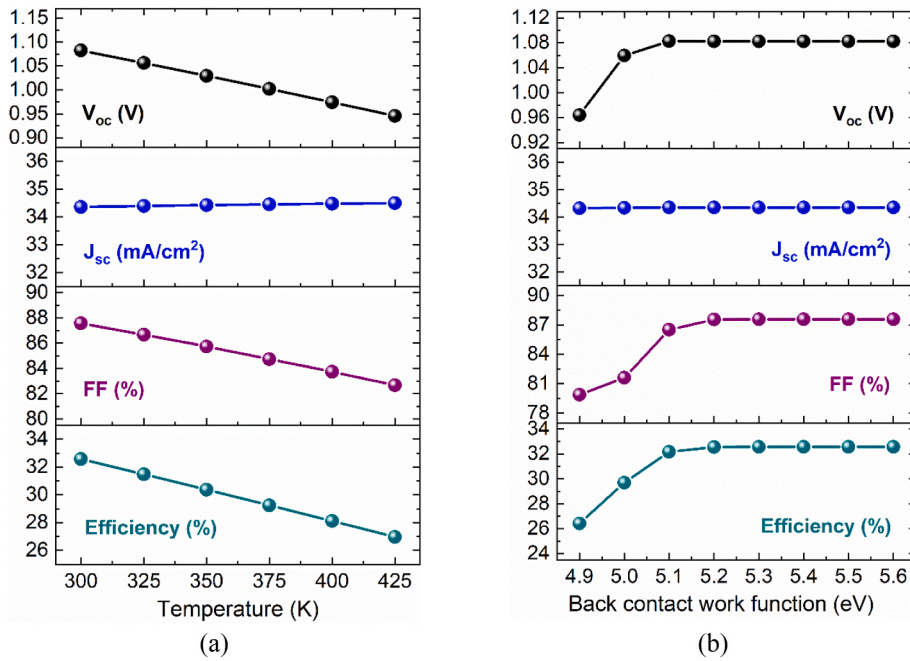


Fig. 13. Impacts of (a) temperature and (b) rear electrode WF on output metrics of the designed PSC.

perovskite increases the carrier recombination rate and expands  $J_0$  [25]. Thus, the value of  $V_{oc}$  drops with the expanding thickness. Therefore, it is essential to determine the appropriate values of  $N_A$  and  $W$  to get the best PV performance from the proposed structure. Here, by considering the fabrication cost and outstanding performance, the  $W$  of 1.0- $\mu\text{m}$  and  $N_A$  value of  $10^{17} \text{ cm}^{-3}$  are selected in our study. At a 1.0- $\mu\text{m}$ -thick  $\text{CH}_3\text{NH}_3\text{SnI}_3$  perovskite layer with a  $N_A$  value of  $10^{17} \text{ cm}^{-3}$ , the highest efficiency of 32.57 %, along with FF of 87.58 %,  $V_{oc}$  of 1.08 V, and  $J_{sc}$  of 34.36 mA/cm<sup>2</sup>, is achieved for the suggested PSC architecture.

### 3.3. Effects of thickness and defect concentration of the $\text{CH}_3\text{NH}_3\text{SnI}_3$ perovskite on device performance

This research further examines the PV outcomes of the recommended  $\text{CH}_3\text{NH}_3\text{SnI}_3$ -based PSC in regards to the thickness ( $W$ ) and bulk defect density ( $N_t$ ). The impact of variations in perovskite layers  $W$  and  $N_t$  ranging from 0.1 to 1.5  $\mu\text{m}$  and  $10^{11}$  to  $10^{17} \text{ cm}^{-3}$  is examined, and the corresponding outcomes are depicted in Fig. 11. According to the figure, it is evident that all the PV output parameters do not vary significantly at the value of  $N_t$  of the  $\text{CH}_3\text{NH}_3\text{SnI}_3$  perovskite layer below  $10^{13} \text{ cm}^{-3}$  and then start to diminish after  $10^{13} \text{ cm}^{-3}$ . One possible explanation for the decline in the performance of the PV devices may be owing to the growth of non-radiative charge recombination in the perovskite layer [56]. Therefore, to obtain superior PV performance, a small number of defects in the perovskite layer must be considered. Hence, in order to improve the PV output metrics of the suggested  $\text{CH}_3\text{NH}_3\text{SnI}_3$ -based PSC, the  $N_t$  of  $10^{14} \text{ cm}^{-3}$  is optimized in this study. Besides, it is obvious that the values of PCE enhance with the expanding  $W$  up to 1.0  $\mu\text{m}$  and then remain almost fixed. In this research, by considering the fabrication cost and superior efficiency, the  $W$  value of 1.0- $\mu\text{m}$  and the  $N_t$  value of  $10^{14} \text{ cm}^{-3}$  are taken for further study. At a 1.0- $\mu\text{m}$ -thick  $\text{CH}_3\text{NH}_3\text{SnI}_3$  perovskite layer with a  $N_t$  value of  $10^{14} \text{ cm}^{-3}$ , the highest efficiency of 32.57 %, along with FF of 87.58 %,  $V_{oc}$  of 1.08 V, and  $J_{sc}$  of 34.36 mA/cm<sup>2</sup>, is obtained for the proposed configuration.

### 3.4. Impacts of interface defect density on cell performances

In this study, numerical analysis is utilized to evaluate the impact of defects at the  $\text{ZnS}/\text{CH}_3\text{NH}_3\text{SnI}_3$  and  $\text{CH}_3\text{NH}_3\text{SnI}_3/\text{MoO}_3$  interfaces

within the proposed heterojunction CIGS PSC. The defect concentration at the interfaces varies from  $10^9$  to  $10^{16} \text{ cm}^{-2}$ . The influence of defect states at the  $\text{ZnS}/\text{CH}_3\text{NH}_3\text{SnI}_3$  interface on device performance parameters is depicted in Fig. 12(a). The figure indicates that performance characteristics remain unchanged until the defect concentration exceeds  $10^{13} \text{ cm}^{-2}$ . As the defect concentration increases from  $10^{13}$  to  $10^{16} \text{ cm}^{-2}$ , the power conversion efficiency (PCE) decreases from 32.57 % to 30.26 %, and  $V_{oc}$  shrinks from 1.08 V to 1.02 V. This decline in efficiency is ascribed to elevated carrier recombination caused by the higher defect density at the interface [26,57]. The results indicate that defects at the  $\text{ZnS}/\text{CH}_3\text{NH}_3\text{SnI}_3$  interface significantly affect the PV device's output. To enhance the PCE of the  $\text{CH}_3\text{NH}_3\text{SnI}_3$  PSC, an optimal defect state of  $10^{12} \text{ cm}^{-2}$  is employed at the  $\text{ZnS}/\text{CH}_3\text{NH}_3\text{SnI}_3$  interface.

Furthermore, how the interface defect between HTL and absorber affects the entire performance of the  $\text{CH}_3\text{NH}_3\text{SnI}_3$  PSC cell is also examined. The effect of defect concentration at the  $\text{CH}_3\text{NH}_3\text{SnI}_3/\text{MoO}_3$  interface on performance parameters such as PCE, FF,  $V_{oc}$ , and  $J_{sc}$  is depicted in Fig. 12(b). It can be observed that, while the defect state of the interface ranges from  $10^9$  to  $10^{16} \text{ cm}^{-2}$ , all the performance parameters become independent until  $10^{13} \text{ cm}^{-2}$ . When the defect is increased from  $10^{13}$  to  $10^{16} \text{ cm}^{-2}$ , the efficiency is decreased from 32.57 % to 27.81 %, FF drops from 87.58 to 85.40 %,  $V_{oc}$  has decreased from 1.08 V to 1.03 V, and lastly,  $J_{sc}$  is diminished from 34.36 mA/cm<sup>2</sup> to 31.35 mA/cm<sup>2</sup>, respectively. Thus, the disparity in defects at the  $\text{CH}_3\text{NH}_3\text{SnI}_3/\text{MoO}_3$  interface profoundly influences device performance [26]. In this theoretical investigation, the suggested  $\text{CH}_3\text{NH}_3\text{SnI}_3$  cell structure with  $\text{MoO}_3$  HTL provides better performance when a defect density of  $10^{12} \text{ cm}^{-2}$  is applied at the interface.

### 3.5. Influences of temperature and rear contact work function on PV output characteristics

The operating temperature has a significant impact on the performance of PSCs. Hence, it is essential to examine the effects of temperature on  $\text{CH}_3\text{NH}_3\text{SnI}_3$ -based PSCs in our study. Here, the corresponding performance parameters regarding the variation of temperature are depicted in Fig. 13(a). We observe that as the temperature decreases, all performance parameters, except for the  $J_{sc}$ , show an improvement. Enhancing the temperature of the PV device prompts a rise in the reverse

**Table 5**

An overview of the dataset used in this ML model.

Samples	Thickness	Band Gap	Electron Affinity	Dielectric Permittivity	Acceptor Density	Defect Density	CB effective DOS	VB effective DOS	PCE
1	0.5	1.3	4.15	8	$1.00 \times 10^{15}$	$1.00 \times 10^{12}$	$1.00 \times 10^{17}$	$5.00 \times 10^{17}$	36.592
2	0.5	1.3	4.15	12	$1.00 \times 10^{15}$	$1.00 \times 10^{12}$	$1.00 \times 10^{17}$	$5.00 \times 10^{17}$	36.5
...	...	...	...	...	...	...	...	...	...
740	1.7	1.55	4.4	18	$5.00 \times 10^{18}$	$1.00 \times 10^{17}$	$5.00 \times 10^{19}$	$1.00 \times 10^{20}$	0.094

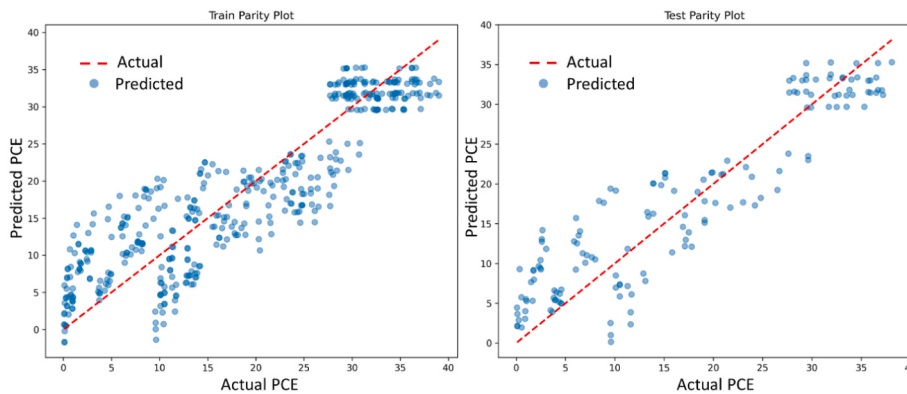


Fig. 14. Parity plot for train and test data for the proposed PSC.

saturation current, which in turn causes a reduction in the  $V_{oc}$  [58]. Further, a rise in temperature results in a slight improvement in the  $J_{sc}$ . This is because higher temperatures generate more electron-hole pairs. However, the recombination process between energy bands also intensifies. The modest increase in  $J_{sc}$  may be attributed to the narrowing of the semiconductor band gaps in the solar cell at elevated temperatures, which ultimately results in a decrease in the  $V_{oc}$  [59,60]. As a result, the drop in  $V_{oc}$  and the negligible rise in  $J_{sc}$  contribute to a decline in the fill factor (FF) and PCE of the solar device when subjected to higher temperatures [6]. In this study, as depicted in Fig. 13(a), the temperature was increased from 300K to 425K. With the rise in temperature, a significant change in the  $V_{oc}$  is observed, dropping from 1.08 V to 0.94 V. Additionally, the efficiency and FF decrease from 32.57 % to 26.96 % and from 87.58 % to 82.67 %, respectively, at temperatures of 300K and 425K. Meanwhile, the  $J_{sc}$  remained relatively stable, hovering around 34.35 mA/cm<sup>2</sup>. Similar findings regarding temperature-sensitive performance metrics of SCs have been reported in earlier researches [19, 21,61].

In this numerical study, we also investigated the influence of the rear electrode's WF on the CH<sub>3</sub>NH<sub>3</sub>SnI<sub>3</sub> PV device. An appropriate back electrode ensures efficient carrier flow and minimizes resistance, which is crucial for high performance and efficiency. To identify a proper rear electrode, WF is ranged from 4.9 eV to 5.6 eV by keeping all the parameters independent, and the effect of work function is illustrated in Fig. 13(b). The figure demonstrates that all the performance parameters, with the exception of  $J_{sc}$ , rise until the WF reaches around 5.2 eV and then remains unaltered. As the work function increases, an ohmic contact replaces the Schottky contact at the back contact of the heterostructure, thereby improving hole transport from the absorber [25]. Enhancing the work function lowers the potential barrier height, thereby ensuring more efficient carrier transport from the absorber. Therefore, in our study, we have selected gold (Au) as the back electrode owing to its high WF of 5.47 eV [36].

### 3.6. Device performances through ML algorithm

In this theoretical study, the SCAPS-1D simulation software has been utilized to produce primary datasets. Table 5 depicts the dataset employed in this model. Here, the number of samples used is 740 and is

**Table 6**

A summary of the ML model performance.

Performance metric	Training	Selection	Testing
Mean squared error	0.279	2.160	1.766
Root mean squared error	0.528	1.470	1.330
correlation coefficient, R <sup>2</sup>	0.898	0.865	0.878

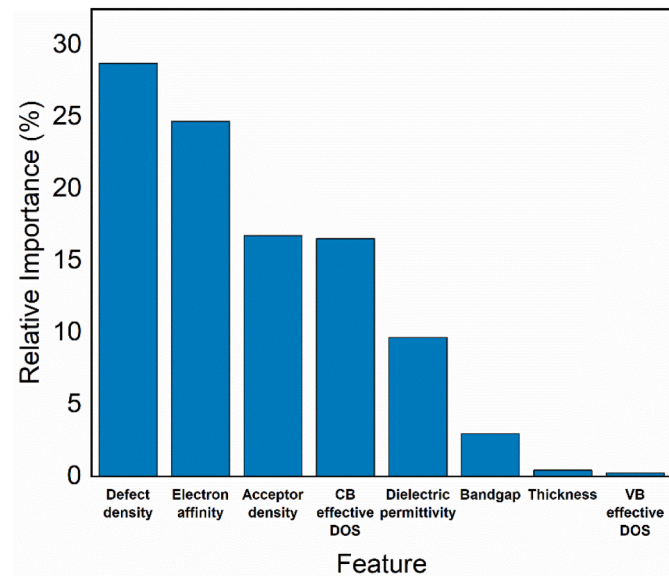


Fig. 15. The relative importance of material properties on the target efficiency.

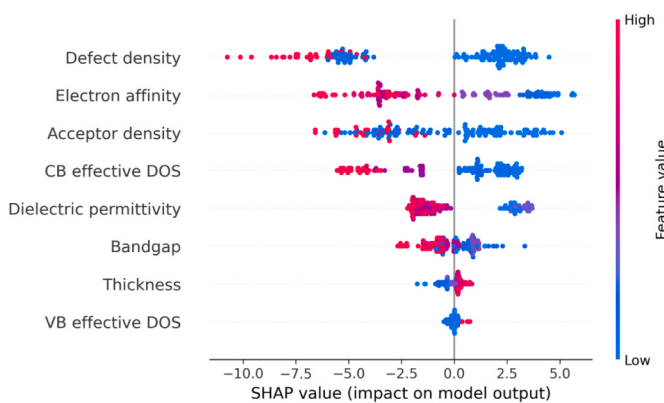
split into 444 (60 %) training, 148 (20 %) selection, and the remaining 148 (20 %) testing samples.

Graphical representations known as parity plots were produced to visually evaluate the model's performance by contrasting actual and predicted values for both the training and testing datasets, as demonstrated in Fig. 14 [29]. These parity graphs offer a visual representation of the linear regression model's efficacy. If both graphs manifest a compact cluster around the red dashed line, it indicates that the model

**Table 7**

Relative percentage importance of input parameters with the target efficiency.

Features	Relative importance (%)
Defect density ( $N_D$ )	28.72
Electron affinity ( $X$ )	24.70
Acceptor density ( $N_A$ )	16.743
CB effective DOS ( $N_c$ )	16.532
Dielectric permittivity ( $\epsilon_r$ )	9.66
Bandgap ( $E_g$ )	2.974
Thickness ( $W$ )	0.436
VB effective DOS ( $N_v$ )	0.240

**Fig. 16.** Impact of material properties on model output.

has effectively gleaned insights from the training dataset and is also adeptly extrapolating to the testing dataset. For an ideal fit, the value of  $R^2$  would be 1. In our case, the values of  $R^2$  are 0.898 and 0.878 for both the training and testing data, which is very close to 1. Additionally, the best performance of the ML algorithm may be expected for training, selection, and testing data when the lowest probable values of MSE and RMSE are identified. The ML model's error metrics are provided in

**Table 8**

Numerous physical parameters optimized for the suggested  $\text{CH}_3\text{NH}_3\text{SnI}_3$  PSC.

Parameters (unit)	ZnS ETL	$\text{CH}_3\text{NH}_3\text{SnI}_3$ Absorber	MoO <sub>3</sub> HTL	Interface defect density	
				$\text{CH}_3\text{NH}_3\text{SnI}_3/\text{ZnS}$	$\text{MoO}_3/\text{CH}_3\text{NH}_3\text{SnI}_3$
Thickness ( $\mu\text{m}$ )	0.05	1.0	0.1		
$N_D$ ( $\text{cm}^{-3}$ )	$10^{18}$	—	—		
$N_A$ ( $\text{cm}^{-3}$ )	—	$10^{17}$	$10^{18}$		
$N_t$ ( $\text{cm}^{-3}$ )	$10^{15}$	$10^{14}$	$10^{15}$		
$\sigma_{n,p}$ ( $\text{cm}^2$ )				$10^{-19}$	$10^{-19}$
Total density ( $\text{cm}^{-2}$ )				$10^{12}$	$10^{12}$

**Table 9**

Variance of efficiencies measured experimentally and numerically for  $\text{CH}_3\text{NH}_3\text{SnI}_3$ -based PSCs.

Structures	Research Area	Efficiency (%)	References
FTO/TiO <sub>2</sub> /CH <sub>3</sub> NH <sub>3</sub> SnI <sub>3</sub> +TiO <sub>2</sub> /Spiro-OMeTAD	Experimental	5.23	[24]
FTO/TiO <sub>2</sub> /CH <sub>3</sub> NH <sub>3</sub> SnI <sub>3</sub> +TiO <sub>2</sub> /Spiro-OMeTAD	"	6.40	[4]
FTO/ZnO/CH <sub>3</sub> NH <sub>3</sub> SnI <sub>3</sub> /CuO	Theoretical	15.10	[62]
FTO/TiO <sub>2</sub> /CH <sub>3</sub> NH <sub>3</sub> SnI <sub>3</sub> /Spiro-OMeTAD	"	23.36	[63]
ITO/SnO <sub>2</sub> /CH <sub>3</sub> NH <sub>3</sub> SnI <sub>3</sub> /CuSCN/Mo	"	23.57	[17]
FTO/TiO <sub>2</sub> /CH <sub>3</sub> NH <sub>3</sub> SnI <sub>3</sub> /CuO	"	26.92	[2]
FTO/TiO <sub>2</sub> /CH <sub>3</sub> NH <sub>3</sub> SnI <sub>3</sub> /CuSbS <sub>2</sub>	"	29.74	[21]
TCO/TiO <sub>2</sub> /CH <sub>3</sub> NH <sub>3</sub> SnI <sub>3</sub> /CuI	"	32.13	[3]
FTO/ZnS/CH <sub>3</sub> NH <sub>3</sub> SnI <sub>3</sub> /MoO <sub>3</sub>	"	32.57	This work

**Table 6.**

To determine which material parameters have the greatest influence on solar cell performance, it is crucial to evaluate the comparative significance of the material properties of the proposed PV cell [29,31,46]. The outcomes obtained are demonstrated in Fig. 15 and summarized in Table 7. Here, the most significant attribute is the defect density, with a relative importance of 28.72 %, which influences the device performance profoundly.

In this study, the influence of each feature on the model's output is further evaluated by using the SHAP (SHapley Additive exPlanations) plot, which is illustrated in Fig. 16. This plot is particularly useful for pinpointing which physical parameters of the elements are most influential in regulating the target variable [29,48]. The X-axis (SHAP value) of the SHAP plot represents the influence of features on the model's prediction, where positive SHAP values elevate and negative SHAP values lower the prediction. On the other hand, the Y-axis lists the features used in the model, arranged by their significance. From the figure, it is evident that the defect density has the highest negative influence on the model's prediction, as indicated by the clustering of red points to the left of the zero line. This suggests that a higher defect density lowers the predicted target value. Therefore, this insightful analysis will be helpful for the researchers of PV technology to design and fabricate highly efficient solar cells with minimal cost and much quicker.

### 3.7. Overall performances of the optimized $\text{CH}_3\text{NH}_3\text{SnI}_3$ -based PSC

In this investigation, we conducted a theoretical analysis to see how different essential parameters of the PV cell affected its performance. The optimized input parameters used for various films in the heterojunction Al/FTO/ZnS/CH<sub>3</sub>NH<sub>3</sub>SnI<sub>3</sub>/MoO<sub>3</sub>/Au PSC appear in Table 8. Additionally, Table 9 compares the efficiencies achieved in previous and current studies for various CH<sub>3</sub>NH<sub>3</sub>SnI<sub>3</sub>-based heterojunction solar cells. We observed a high efficiency of 32.57 %, with a  $V_{oc}$  of 1.08 V,  $J_{sc}$  of 34.35 mA/cm<sup>2</sup>, and FF of 87.57 % for the optimized CH<sub>3</sub>NH<sub>3</sub>SnI<sub>3</sub> PSC with MoO<sub>3</sub> HTL and ZnS ETL. These optimized intrinsic parameters will be useful for scientists in the solar energy field to design and develop highly efficient CH<sub>3</sub>NH<sub>3</sub>SnI<sub>3</sub> perovskite solar cells.

#### 4. Conclusion

In this study, a planner heterostructure eco-friendly Pb-free PSC with the configuration of Al/FTO/ZnS/CH<sub>3</sub>NH<sub>3</sub>SnI<sub>3</sub>/MoO<sub>3</sub>/Au is designed and examined theoretically using the SCAPS-1D simulator. Here, p<sup>+</sup>-type MoO<sub>3</sub> is used as an HTL, and n<sup>+</sup>-type ZnS is used as an ETL. The baseline parameters, including thickness, shallow acceptor density, and bulk defect state of the perovskite layer, are optimized to achieve excellent PV output metrics. Additionally, the impacts of interface defects at the ZnS/CH<sub>3</sub>NH<sub>3</sub>SnI<sub>3</sub> and CH<sub>3</sub>NH<sub>3</sub>SnI<sub>3</sub>/MoO<sub>3</sub> interfaces are carefully examined. Further, Nyquist plots and lattice mismatch calculations are provided to analyze the non-radiative carrier recombination at both interfaces. The influences of temperature and back metal WF on cell performance are also investigated. After optimization of all the material properties, the optimum efficiency of 32.57 %, along with FF of 87.58 %, V<sub>oc</sub> of 1.08 V, and J<sub>sc</sub> of 34.36 mA/cm<sup>2</sup>, is achieved for the presented configuration. Ultimately, a linear regression ML algorithm is trained to investigate the impacts of physical parameters of the perovskite layer on the efficiency of the proposed PSC, and a highest relative importance of 28.72 % is obtained for the bulk defect density of the perovskite layer. These findings indisputably demonstrate that environmentally sound, Pb-free PSCs are an appropriate choice in PV technology. The proposed CH<sub>3</sub>NH<sub>3</sub>SnI<sub>3</sub>-based PSC provides a feasible approach to designing an inexpensive, reliable, and highly efficient solar cell.

#### CRediT authorship contribution statement

**Tanvir Mahtab Khan:** Writing – original draft, Software, Methodology, Investigation, Formal analysis, Conceptualization. **Benjer Islam:** Writing – original draft, Software, Formal analysis. **Md Mountasir Rahaman:** Writing – original draft, Software, Formal analysis. **Mirza Md Shakil:** Writing – original draft, Software, Methodology, Formal analysis. **Md Ferdous Rahman:** Writing – review & editing, Formal analysis. **Sheikh Rashel Al Ahmed:** Writing – review & editing, Supervision, Methodology, Investigation, Conceptualization.

#### Declaration of competing interest

The authors declare that they have no known competing financial interests or personal relationships that could have appeared to influence the work reported in this paper.

#### Acknowledgement

We are very grateful to Marc Burgelman, Electronics and Information Systems (ELIS), University of Gent, Belgium, for providing us with SCAPS-1D software.

#### Data availability

Data will be made available on request.

#### References

- [1] P.K. Patel, Device simulation of highly efficient eco-friendly CH<sub>3</sub>NH<sub>3</sub>SnI<sub>3</sub> perovskite solar cell, *Sci. Rep.* 11 (2021) 3082.
- [2] M. Mottakin, K. Sobayel, D. Sarkar, H. Alkhammash, S. Alharthi, K. Techato, M. Shahiduzzaman, N. Amin, K. Sopian, M. Akhtaruzzaman, Design and modelling of eco-friendly CH<sub>3</sub>NH<sub>3</sub>SnI<sub>3</sub>-based perovskite solar cells with suitable transport layers, *Energies* 14 (2021) 7200.
- [3] S. Imani, S.M. Seyed-Talebi, J. Beheshtian, E.W.G. Diau, Simulation and characterization of CH<sub>3</sub>NH<sub>3</sub>SnI<sub>3</sub>-based perovskite solar cells with different Cu-based hole transporting layers, *Appl. Phys. A* 129 (2023) 143.
- [4] N.K. Noel, S.D. Stranks, A. Abate, C. Wehrenfennig, S. Guarnera, A.-A. Haghhighirad, A. Sadhanala, G.E. Eperon, S.K. Pathak, M.B. Johnston, Lead-free organic-inorganic tin halide perovskites for photovoltaic applications, *Energy Environ. Sci.* 7 (2014) 3061–3068.
- [5] M.S. Salem, A.J. Alzahrani, R.A. Ramadan, A. Alanazi, A. Shaker, M. Abouelatta, C. Gontrand, M. Elbanna, A. Zekry, Physically based analytical model of heavily doped silicon wafers based proposed solar cell microstructure, *IEEE Access* 8 (2020) 138898–138906.
- [6] P. Gao, M. Grätzel, M.K. Nazeeruddin, Organohalide lead perovskites for photovoltaic applications, *Energy Environ. Sci.* 7 (2014) 2448–2463.
- [7] F. Izadi, A. Ghobadi, A. Gharaati, M. Minbashi, A. Hajjiah, Effect of interface defects on high efficient perovskite solar cells, *Optik* 227 (2021) 166061.
- [8] A. Sunny, S. Rahman, M. Khutun, S.R.A. Ahmed, Numerical study of high performance HTL-free CH<sub>3</sub>NH<sub>3</sub>SnI<sub>3</sub>-based perovskite solar cell by SCAPS-1D, *AIP Adv.* 11 (2021).
- [9] Y. Wang, T. Mahmoudi, Y.B. Hahn, Highly stable and efficient perovskite solar cells based on FAMA-perovskite-Cu: NiO composites with 20.7% efficiency and 80.5% fill factor, *Adv. Energy Mater.* 10 (2020) 2000967.
- [10] L. Hao, T. Li, X. Ma, J. Wu, L. Qiao, X. Wu, G. Hou, H. Pei, X. Wang, X. Zhang, A tin-based perovskite solar cell with an inverted hole-free transport layer to achieve high energy conversion efficiency by SCAPS device simulation, *Opt. Quantum Electron.* 53 (2021) 1–17.
- [11] Y. He, L. Xu, C. Yang, X. Guo, S. Li, Design and numerical investigation of a lead-free inorganic layered double perovskite Cs<sub>x</sub>CuSb<sub>2</sub>Cl<sub>12</sub> nanocrystal solar cell by SCAPS-1D, *Nanomater* 11 (2021) 2321.
- [12] Q. Tai, J. Cao, T. Wang, F. Yan, Recent advances toward efficient and stable tin-based perovskite solar cells, *EcoMat* 1 (2019) e12004.
- [13] J. Cao, F. Yan, Recent progress in tin-based perovskite solar cells, *Energy Environ. Sci.* 14 (2021) 1286–1325.
- [14] M. Lazemi, S. Asgharizadeh, S. Bellucci, A computational approach to interface engineering of lead-free CH<sub>3</sub>NH<sub>3</sub>SnI<sub>3</sub> highly-efficient perovskite solar cells, *Phys. Chem. Chem. Phys.* 20 (2018) 25683–25692.
- [15] T. Yokoyama, D.H. Cao, C.C. Stoumpos, T.-B. Song, Y. Sato, S. Aramaki, M. G. Kanatzidis, Overcoming short-circuit in lead-free CH<sub>3</sub>NH<sub>3</sub>SnI<sub>3</sub> perovskite solar cells via kinetically controlled gas-solid reaction film fabrication process, *J. Phys. Chem. Lett.* 7 (2016) 776–782.
- [16] H. Min, D.Y. Lee, J. Kim, G. Kim, K.S. Lee, J. Kim, M.J. Paik, Y.K. Kim, K.S. Kim, M. G. Kim, Perovskite solar cells with atomically coherent interlayers on SnO<sub>2</sub> electrodes, *Nature* 598 (2021) 444–450.
- [17] M.S. Hanif, I. Qasim, M.I. Malik, M.F. Nasir, O. Ahmad, A. Rashid, Development of low-cost and high-efficiency solar modules based on perovskite solar cells for large-scale applications, *Heliyon* 10 (2024) e25703.
- [18] U. Mandadapu, S.V. Vedanayakam, K. Thyagarajan, M.R. Reddy, B. Babu, Design and simulation of high efficiency tin halide perovskite solar cell, *Int. J. Renew. Energy Resour.* 7 (2017) 1603–1612.
- [19] F. Arif, M. Aamir, A. Shuja, M. Shahiduzzaman, J. Akhtar, Simulation and numerical modeling of high performance CH<sub>3</sub>NH<sub>3</sub>SnI<sub>3</sub> solar cell with cadmium sulfide as electron transport layer by SCAPS-1D, *Results Opt.* 14 (2024) 100595.
- [20] K.D. Jayan, V. Sebastian, Comprehensive device modelling and performance analysis of MASnI<sub>3</sub> based perovskite solar cells with diverse ETM, HTM and back metal contacts, *Sol. Energy* 217 (2021) 40–48.
- [21] N.J. Valeti, K. Prakash, M.K. Singha, Numerical simulation and optimization of lead free CH<sub>3</sub>NH<sub>3</sub>SnI<sub>3</sub> perovskite solar cell with CuSbS<sub>2</sub> as HTL using SCAPS 1D, *Results Opt.* 12 (2023) 100440.
- [22] Z. Wang, H. Gao, D. Wu, J. Meng, J. Deng, M. Cui, Defects and defect passivation in perovskite solar cells, *Molecules* 29 (2024) 2104.
- [23] L. Peng, W. Xie, Theoretical and experimental investigations on the bulk photovoltaic effect in lead-free perovskites MASnI<sub>3</sub> and FASnI<sub>3</sub>, *RSC Adv.* 10 (2020) 14679–14688.
- [24] F. Hao, C.C. Stoumpos, D.H. Cao, R.P. Chang, M.G. Kanatzidis, Lead-free solid-state organic-inorganic halide perovskite solar cells, *Nat. Photonics* 8 (2014) 489–494.
- [25] T.M. Khan, S.R.A. Ahmed, Investigating the performance of FASnI<sub>3</sub>-based perovskite solar cells with various electron and hole transport layers: machine learning approach and SCAPS-1D analysis, *Adv. Theory Simul.* 7 (2024) 2400353.
- [26] Y. Cao, X. Zhu, H. Chen, X. Zhang, J. Zhouc, Z. Hu, J. Pang, Towards high efficiency inverted Sb<sub>2</sub>Se<sub>3</sub> thin film solar cells, *Sol. Energy Mater. Sol. Cells* 200 (2019) 109945.
- [27] T.M. Khan, A. Hosen, O. Saidani, S.R. Al Ahmed, Artificial neural network assisted numerical analysis on performance enhancement of Sb<sub>2</sub>(S,Se)<sub>3</sub> solar cell with SnS as HTL, *Mater. Today Commun.* (2024) 109639.
- [28] A. Mellit, S. Kalogirou, Machine learning and deep learning for photovoltaic applications, in: *Artificial Intelligence for Smart Photovoltaic Technologies*, AIP Publishing LLC, Melville, New York, 2022, 1-1-20.
- [29] M.S. Islam, M.T. Islam, S. Sarker, H.A. Jame, S.S. Nishat, M.R. Jani, A. Rauf, S. Ahsan, K.M. Shorowordi, H. Efstathiadis, Machine learning approach to delineate the impact of material properties on solar cell device Physics, *ACS Omega* 7 (2022) 22263–22278.
- [30] F. Li, X. Peng, Z. Wang, Y. Zhou, Y. Wu, M. Jiang, M. Xu, Machine learning (ML)-assisted design and fabrication for solar cells, *Energy Environ. Mater.* 2 (2019) 280–291.
- [31] R. Kundara, S. Baghel, Predictive design of KSnI<sub>3</sub>-based perovskite solar cells using SCAPS and machine learning model, *Mater. Sci. Eng. B* 307 (2024) 117536.
- [32] S.R.A. Ahmed, Investigation on the performance enhancement of heterojunction SnS thin-film solar cell with a Zn<sub>3</sub>P<sub>2</sub> hole transport layer and a TiO<sub>2</sub> electron transport layer, *Energy Fuels* 38 (2023) 1462–1476.
- [33] M.A. Rahman, Enhancing the photovoltaic performance of Cd-free Cu<sub>2</sub>ZnSnS<sub>4</sub> heterojunction solar cells using SnS HTL and TiO<sub>2</sub> ETL, *Sol. Energy* 215 (2021) 64–76.

- [34] M.M. Khatun, A. Hosen, S.R. Al Ahmed, Evaluating the performance of efficient  $\text{Cu}_2\text{NiSnS}_4$  solar cell—a two stage theoretical attempt and comparison to experiments, *Heliyon* 9 (2023) e20603.
- [35] T.M. Khan, M.M. Khatun, H. Khatun, A. Hosen, S.R. Al Ahmed, Design and simulation of a highly efficient SnSe solar cell with CuI as an HTL by SCAPS-1D, in: 2023 IEEE International Conference on Telecommunications and Photonics (ICTP), IEEE, 2023, pp. 1–5.
- [36] H.B. Michaelson, The work function of the elements and its periodicity, *J. Appl. Phys.* 48 (1977) 4729–4733.
- [37] A. Hosen, S. Yeasmin, K.S.B. Rahmotullah, M.F. Rahman, S.R. Al Ahmed, Design and simulation of a highly efficient  $\text{CuBi}_2\text{O}_4$  thin-film solar cell with hole transport layer, *Opt. Laser. Technol.* 169 (2024) 110073.
- [38] A. Das, S.D. Peu, M.A.M. Akanda, M.M. Salah, M.S. Hossain, B.K. Das, Numerical simulation and optimization of inorganic lead-free  $\text{Cs}_3\text{Bi}_2\text{I}_9$ -based perovskite photovoltaic cell: impact of various design parameters, *Energies* 16 (2023) 2328.
- [39] S. Li, Y.-L. Cao, W.-H. Li, Z.-S. Bo, A brief review of hole transporting materials commonly used in perovskite solar cells, *Rare Met.* 40 (2021) 2712–2729.
- [40] M. Gloeckler, J. Sites, Efficiency limitations for wide-band-gap chalcocyanide solar cells, *Thin Solid Films* 480 (2005) 241–245.
- [41] B. Islam, A. Hosen, T.M. Khan, M.F. Rahman, M.H. Rahman, M.S. Islam, S.R. A. Ahmed, Simulating the effect of inserting  $\text{Sb}_2\text{S}_3$  as hole transport layer on SnS-based thin-film solar cells, *J. Electron. Mater.* (2024) 1–14.
- [42] K. Sekar, L. Marasamy, S. Mayarambakkam, P. Selvarajan, J. Bouclé, Highly efficient lead-free silver bismuth iodide ( $\text{Ag}_3\text{BiI}_6$ ) Ruddlesden-Popper solar cells with novel device architecture: a numerical study, *Mater. Today Commun.* (2024) 108347.
- [43] S. Datta, A. Baul, G.C. Sarker, P.K. Sadhu, D.R. Hodges, A comprehensive review of the application of machine learning in fabrication and implementation of photovoltaic systems, *IEEE Access* 11 (2023) 77750–77778.
- [44] T.J. Jacobsson, A. Hultqvist, A. García-Fernández, A. Anand, A. Al-Ashouri, A. Hagfeldt, A. Crovetto, A. Abate, A.G. Ricciardulli, A. Vijayan, An open-access database and analysis tool for perovskite solar cells based on the FAIR data principles, *Nat. Energy* 7 (2022) 107–115.
- [45] M. Bansal, A. Goyal, A. Choudhary, A comparative analysis of K-nearest neighbor, genetic, support vector machine, decision tree, and long short term memory algorithms in machine learning, *Decis. Anal. J.* 3 (2022) 100071.
- [46] M.M. Salah, Z. Ismail, S. Abdellatif, Selecting an appropriate machine-learning model for perovskite solar cell datasets, *Mater. Renew. Sustain. Energy* 12 (2023) 187–198.
- [47] M.A. Iqbal, Application of regression techniques with their advantages and disadvantages, *Elektron Mag* 4 (2021) 11–17.
- [48] N. Kaur, R. Pandey, M.K. Hossain, J. Madan, Machine learning-aided optimization for transport layer parameters of low lead inorganic Zn-based mixed-halide perovskite solar cell, *Sol. Energy* 264 (2023) 112055.
- [49] T. Song, A. Kanevce, J.R. Sites, Emitter/absorber interface of CdTe solar cells, *J. Appl. Phys.* 119 (2016).
- [50] L.-L. Wu, G.-W. Wang, J. Tian, D.-M. Wang, D.-L. Wang, Recombination-induced voltage-dependent photocurrent collection loss in CdTe thin film solar cell, *Chin. Phys. B* 31 (2022) 108803.
- [51] H. Wilhelm, H.-W. Schock, R. Scheer, Interface recombination in heterojunction solar cells: influence of buffer layer thickness, *J. Appl. Phys.* 109 (2011).
- [52] X. Wang, R. Tang, C. Jiang, W. Lian, H. Ju, G. Jiang, Z. Li, C. Zhu, T. Chen, Manipulating the electrical properties of  $\text{Sb}_2(\text{S},\text{Se})_3$  film for high-efficiency solar cell, *Adv. Energy Mater.* 10 (2020) 2002341.
- [53] K. Sekar, L. Marasamy, S. Mayarambakkam, H. Hawashin, M. Nour, J. Bouclé, Lead-free, formamidinium germanium-antimony halide ( $\text{FA}_4\text{GeSbCl}_3$ ) double perovskite solar cells: the effects of band offsets, *RSC Adv.* 13 (2023) 25483–25496.
- [54] B.A. Odeke, G.D. Chung, J.A. Fajemisin, K.S. Suraj, D.K. Tonui, A.R. Tobi, T. C. Bewaa, J.A. Ajibola, N.Y. Dzade, Electronic structure and surface properties of copper thiocyanate: a promising hole transport material for organic photovoltaic cells, *Materials* 13 (2020) 5765.
- [55] I. Alam, R. Mollick, M.A. Ashraf, Numerical simulation of  $\text{Cs}_2\text{AgBiBr}_6$ -based perovskite solar cell with  $\text{ZnO}$  nanorod and P3HT as the charge transport layers, *Phys. B Condens. Matter* 618 (2021) 413187.
- [56] Y. Xiao, H. Wang, H. Kuang, Numerical simulation and performance optimization of  $\text{Sb}_2\text{S}_3$  solar cell with a hole transport layer, *Opt. Mater.* 108 (2020) 110414.
- [57] Y. Wang, Z. Xia, J. Liang, X. Wang, Y. Liu, C. Liu, S. Zhang, H. Zhou, Towards printed perovskite solar cells with cuprous oxide hole transporting layers: a theoretical design, *Semicond. Sci. Technol.* 30 (2015) 054004.
- [58] A. Bouich, B. Hartiti, S. Ullah, H. Ullah, M.E. Touhami, D. Santos, B. Mari, Experimental, theoretical, and numerical simulation of the performance of  $\text{CuIn}_x\text{Ga}_{(1-x)}\text{S}_2$ -based solar cells, *Optik* 183 (2019) 137–147.
- [59] Y.P. Varshni, Temperature dependence of the energy gap in semiconductors, *Phys. 34* (1967) 149–154.
- [60] P. Singh, N.M. Ravindra, Temperature dependence of solar cell performance—an analysis, *Sol. Energy Mater. Sol. Cells* 101 (2012) 36–45.
- [61] A. Laoudi, A.A. Belghiti, K. Wisniewski, A. Abouais, M. Tlemçani, P. Plöciennik, A. Hajjaji, A. Zawadzka, Enhancing the efficiency and stability of Non\_Toxic  $\text{RbSn}_{0.5}\text{Ge}_{0.5}\text{I}_3$ -Based perovskite solar cells through optimization, *Mater. Sci. Eng. B* 310 (2024) 117672.
- [62] E. Danladi, A.O. Salawu, M.O. Abdulmalik, E.D. Onwoke, D. S. Adepehin, Optimization of absorber and ETM layer thickness for enhanced tin based perovskite solar cell performance using SCAPS-1D software, *Phys. Access* 2 (2022) 1–11.
- [63] H.-J. Du, W.-C. Wang, J.-Z. Zhu, Device simulation of lead-free  $\text{CH}_3\text{NH}_3\text{SnI}_3$  perovskite solar cells with high efficiency, *Chin. Phys. B* 25 (2016) 108802.